

# NEW FEEDBACK CONTROL AND ADAPTIVE EVOLVE-FILTER-RELAX REGULARIZATION FOR THE NAVIER-STOKES EQUATIONS IN THE CONVECTION-DOMINATED REGIME

MARIA STRAZZULLO<sup>1</sup>, FRANCESCO BALLARIN<sup>2</sup>, TRAIAN ILIESCU<sup>3</sup>, CLAUDIO CANUTO<sup>1</sup>

**ABSTRACT.** We propose, analyze, and investigate numerically a novel feedback control strategy for high Reynolds number flows. For both the continuous and the discrete (finite element) settings, we prove that the new strategy yields accurate results for high Reynolds numbers that were not covered by current results. We also show that the new feedback control yields more accurate results than the current control approaches in marginally-resolved numerical simulations of a two-dimensional flow past a circular cylinder at Reynolds numbers  $Re = 1000$ . We note, however, that for realistic control parameters, the stabilizing effect of the new feedback control strategy is not sufficient in the convection-dominated regime. Our second contribution is the development of an adaptive evolve-filter-relax (aEFR) regularization that stabilizes marginally-resolved simulations in the convection-dominated regime and increases the accuracy of the new feedback control in realistic parameter settings. For the finite element setting, we prove that the novel feedback control equipped with the new aEFR method yields accurate results for high Reynolds numbers. Furthermore, our numerical investigation shows that the new strategy yields accurate results for reduced order models that dramatically decrease the size of the feedback control problem.

## 1. INTRODUCTION

Flow control is central in numerous applications [34]. The scientific interest in optimal and sub-optimal control strategies for the Navier-Stokes equations is amply documented in the literature, see, for example, [9, 10, 11, 13, 14, 19, 26, 35, 36, 37, 39, 40, 61, 62, 63]. The main goal of flow control is to steer the fluid toward a desired configuration. For laminar flows, flow control strategies (e.g., feedback control) have been successful at both the theoretical and the computational levels. Turbulent flows, however, still pose significant challenges to classical flow control approaches. One of these challenges is the convection-dominated regime, in which under-resolved or marginally-resolved full order models (FOMs), i.e., computational models obtained with classical numerical discretizations (e.g., the finite element method), yield inaccurate results, usually in the form of numerical oscillations. Furthermore, although the flow control strategies generally have a stabilizing effect on the underlying numerical simulations, this is often not sufficient to stabilize the simulations for realistic control parameters. Another significant challenge for flow control of turbulent flows is the high computational cost of FOMs. Indeed, resolving all the spatial scales in a turbulent flow, down to the Kolmogorov scale, can require billions of degree of freedom, which makes the repeated FOM simulation in a control setting impractical.

In this paper, we propose strategies for enabling an efficient and accurate feedback control of convection-dominated flows modeled by the Navier-Stokes equations. Our first contribution is a novel feedback control algorithm for high Reynolds number flows. For both the continuous and the finite element settings, we prove that the new feedback control yields accurate results for high Reynolds numbers that were not covered by current results. This significant improvement over the current feedback control strategies is enabled by introducing a new control forcing term that

<sup>1</sup> POLITECNICO DI TORINO, DEPARTMENT OF MATHEMATICAL SCIENCES “GIUSEPPE LUIGI LAGRANGE”, CORSO DUCA DEGLI ABRUZZI, 24, 10129, TORINO, ITALY

<sup>2</sup>DEPARTMENT OF MATHEMATICS AND PHYSICS, CATHOLIC UNIVERSITY OF THE SACRED HEART, VIA MUSEI 41, I-25121 BRESCIA, ITALY

<sup>3</sup>DEPARTMENT OF MATHEMATICS, VIRGINIA TECH, BLACKSBURG, VA 24061, USA

*Date:* July 4, 2023.

avoids the strict constraints imposed on the Reynolds number at a theoretical level in current approaches [33]. Furthermore, we show that the new feedback control yields more accurate results than the current control approaches in marginally-resolved numerical simulations.

Despite its improved theoretical and numerical properties, the new feedback control yields inaccurate results in the convection-dominated regime when realistic control parameters are used, i.e., when the control action is weaker. We note that, although the control can be often seen as a stabilizer since it steers the approximation to the steady state solution [10, 11, 62, 63], the convection-dominated regime poses additional stability challenges [17]. To address the numerical instability of the new feedback control, we propose an adaptive regularization, which leverages spatial filtering to increase the stability of the new feedback control. The novel *adaptive evolve-filter-relax (aEFR)* strategy consists of three simple steps: (i) Evolve the current velocity to the next step using the standard FOM discretization. (ii) Filter the intermediate FOM approximation obtained in step (i). (iii) Relax the filtered intermediate approximation obtained in step (ii). Steps (i)–(iii) are repeated until a good agreement with the desired state is reached. The aEFR approximation at the next time step is precisely the relaxed approximation obtained in step (iii). The aEFR algorithm has two appealing properties: (a) aEFR is one of the simplest stabilized strategies. Indeed, one can start with a FOM code, add a simple filtering function (described in section 4.2), and obtain the aEFR code in a matter of minutes. (b) The three steps of the aEFR algorithm (i.e., running the FOM algorithm for one step to get the intermediate solution, filtering this intermediate solution, and then relaxing it) are highly modular. For the finite element setting, we prove and show numerically that the novel feedback control equipped with the new aEFR method yields accurate results for high Reynolds numbers.

The new feedback control and aEFR strategies address the numerical instability of classical flow control strategies for convection-dominated flows. To address the high computational cost of current flow control approaches, we propose reduced order models (ROMs), which represent an appealing alternative to the expensive FOMs since the ROM dimensions can be orders of magnitude lower than the FOM dimensions. The following is a far from complete list of papers in which ROMs have been used in control of linear and nonlinear systems [2, 3, 4, 8, 20, 21, 23, 42, 43, 44, 47, 52, 53, 59, 68, 69, 70], and, in particular, control of the Navier-Stokes equations [5, 6, 13, 40, 56, 72]. Galerkin ROMs (G-ROMs), which leverage data to build the basis in the Galerkin framework, have been successful in the numerical simulation of laminar flows. However, for turbulent flows, under-resolved G-ROMs yield inaccurate results, usually in the form of spurious numerical oscillations. Just as in the FOM case, to alleviate these numerical oscillations, stabilized ROMs [27, 28, 29, 30, 31, 32, 41, 55, 65, 67, 75] are generally used. In this paper, we leverage the aEFR strategy to stabilize the ROM simulations. Furthermore, we use the resulting aEFR-ROM within the new feedback control setting to ensure both the accuracy and the efficiency of flow control for convection-dominated flows. We note that, despite their appeal (and the use of regularized FOMs for control [50]), to the best of our knowledge, regularized ROMs (such as aEFR-ROM) have never been used for flow control (see, however, [18, 48, 76, 77] for different FOM and ROM stabilization approaches for optimal control).

The rest of the paper is organized as follows: in section 2, we present the EFR strategy at both the FOM and the ROM levels. In section 3, we first present the current feedback control approach and then propose a novel feedback control strategy that targets higher Reynolds number flows. For both feedback control approaches, we consider both the continuous and the discrete cases. At the FOM level, we prove that the new feedback control is accurate at higher Reynolds numbers for which the theoretical results for the standard control do not hold. In section 4, we propose the new aEFR strategy that further increases the numerical stability of the novel feedback control and enables it to accurately approximate convection-dominated flows for realistic, weak control action. In section 5, we first numerically investigate the improvement of the new feedback control strategy over the current approach at the FOM level. Then, we extend the new feedback control strategy to the EFR setting both at the FOM and ROM level. Furthermore, we show that, using the novel feedback control framework in the numerical simulation of a flow past a cylinder at Reynolds number 1000, the EFR and aEFR strategies yield more accurate results than the standard noEFR approach.

In section 6, we draw conclusions and outline possible research directions. Finally, in Appendix A, we present results that show the positive effect of the EFR strategy at both the FOM and the ROM levels.

## 2. THE EVOLVE-FILTER-RELAX (EFR) STRATEGY FOR FOM AND ROM

In this section, we present the EFR strategy. For the sake of brevity, we limit the discussion only to the algorithmic viewpoint and refer the reader to, e.g., [71, 74] for more details. In Appendix A, we provide numerical evidence in favor of the use of EFR techniques in the full and reduced settings. In what follows, we use the same acronyms as those used in [71]:

- noEFR denotes the FOM in which the EFR regularization is not used.
- EFR denotes the FOM in which the EFR regularization is used.
- EFR-noEFR denotes the ROM in which the EFR regularization is used at the FOM level but not at the ROM level.
- EFR-EFR denotes the ROM in which the EFR regularization is used both at the FOM and the ROM levels.

**2.1. Navier-Stokes Equations.** In this section, we present the incompressible Navier-Stokes equations (NSE), which are the mathematical model used in theoretical and numerical investigations. Let  $\Omega \subset \mathbb{R}^2$  be the spatial domain. We seek to approximate the velocity  $u(x, t) \doteq u \in \mathbb{U} \doteq L^2((0, T); H_{u_D}^1(\Omega))$  and pressure  $p(x, t) \doteq p \in \mathbb{Q} \doteq L^2((0, T); L^2(\Omega))$  [58]:

$$(1) \quad \begin{cases} u_t - \nu \Delta u + (u \cdot \nabla)u + \nabla p = 0 & \text{in } \Omega \times (0, T), \\ \nabla \cdot u = 0 & \text{in } \Omega \times (0, T), \\ u = u_D & \text{on } \Gamma_D \times (0, T), \\ -pn + \nu \frac{\partial u}{\partial n} = 0 & \text{on } \Gamma_N \times (0, T), \\ u(x, 0) = u_0 & \text{in } \Omega, \end{cases}$$

where  $u_0$  is a given initial condition in  $\Omega$ ,  $u_D$  is a given boundary condition on  $\Gamma_D$ , and  $\Gamma_D$  and  $\Gamma_N$  are the portions of the domain featuring Dirichlet and “free flow” boundary conditions, respectively, with  $\Gamma_D \cup \Gamma_N = \partial\Omega$ ,  $\Gamma_D \cap \Gamma_N = \emptyset$ . Moreover,  $\nu$  is the kinematic viscosity and  $n$  represents the outer normal vector to  $\Gamma_N$ . The space  $H_{u_D}^1(\Omega)$  contains functions in  $H^1(\Omega)$  that satisfy the Dirichlet boundary condition.

Denoting by  $\bar{U}$  and  $L$  the characteristic velocity and length scales of the problem at hand, we define the Reynolds number as

$$(2) \quad Re \doteq \frac{\bar{U}L}{\nu}.$$

Large Reynolds numbers determine a convection-dominated regime, where inertial forces dominate the viscous forces.

**2.2. The EFR Strategy.** Convection-dominated regimes generally lead to spurious numerical oscillations in under-resolved or marginally-resolved discretizations, i.e., when the spatial resolution is larger than the Kolomogorov lengthscale, which decreases with the Reynolds number [25, 57]. The EFR algorithm is a numerical stabilization strategy that can alleviate this issue. Let us consider  $\Delta t$  as time step. Thus,  $t_n = n\Delta t$  for  $n = 0, \dots, N_T$ , and  $T = N_T\Delta t$ . Let us denote the FE velocity  $u^h(t) \in \mathbb{U}^{N_h^u}$  and the FE pressure  $p^h \in \mathbb{Q}^{N_h^p}$ , where  $N_h^u$  and  $N_h^p$  denote the FE dimension of the two spaces. We call  $u^n$  and  $p^n$  the FE variables  $u^h(t)$  and  $p^h(t)$  evaluated at  $t^n$ . Using the implicit Euler

discretization in time, with the relaxation parameter  $\chi \in (0, 1)$ , the EFR at the time  $t^{n+1}$  reads:

$$\begin{aligned}
\text{(I)} \quad \textit{Evolve:} \quad & \begin{cases} \frac{\tilde{u}^{n+1} - u^n}{\Delta t} + (\tilde{u}^{n+1} \cdot \nabla) \tilde{u}^{n+1} - \nu \Delta \tilde{u}^{n+1} + \nabla p^{n+1} = 0 & \text{in } \Omega, \\ \nabla \cdot \tilde{u}^{n+1} = 0 & \text{in } \Omega, \\ \tilde{u}^{n+1} = u_D^{n+1} & \text{on } \Gamma_D, \\ -p^{n+1} n + \nu \frac{\partial \tilde{u}^{n+1}}{\partial n} = 0 & \text{on } \Gamma_N. \end{cases} \\
\text{(II)} \quad \textit{Filter:} \quad & \begin{cases} -\delta^2 \Delta \bar{u}^{n+1} + \bar{u}^{n+1} = \tilde{u}^{n+1} & \text{in } \Omega, \\ \bar{u}^{n+1} = u_D^{n+1} & \text{on } \Gamma_D, \\ \frac{\partial \bar{u}^{n+1}}{\partial n} = 0 & \text{on } \Gamma_N. \end{cases} \\
\text{(III)} \quad \textit{Relax:} \quad & u^{n+1} = (1 - \chi) \tilde{u}^{n+1} + \chi \bar{u}^{n+1}.
\end{aligned}$$

In step (I), the velocity approximation  $u^n$  at the current time is evolved to  $\tilde{u}^{n+1}$ , which is the intermediate velocity approximation at the new time,  $t^{n+1}$ . In step (II), a *differential filter* (DF) with filtering radius  $\delta$  is used to filter the intermediate velocity approximation,  $\tilde{u}^{n+1}$ , obtained in step (I). The DF alleviates oscillations by leveraging an elliptic operator that eliminates the high frequencies from  $\tilde{u}^{n+1}$ . In step (III), the filtered velocity is relaxed in order to diminish the diffusion action [22, 24, 51] and increase the accuracy of the simulation: the reader may refer to [15] and [22] for numerical and theoretical results, respectively. We stress that other filters might be employed in the EFR algorithm (see, for example, [27] and the references therein). In our approach, we followed the strategy used in [71].

**2.3. The EFR-noEFR approach.** In this section, we present the EFR-noEFR approach, i.e., we use the EFR stabilization at the FOM level (as described in section 2.2), but at the ROM level we use the standard ROM (without EFR stabilization). POD-based ROM algorithms build reduced spaces based on data compression of the *snapshots*, i.e., FOM simulations collected at specific time instances. Consider two sets of basis functions, for velocity and pressure, respectively,  $\{\phi_j\}_{j=1}^{r_u}$  and  $\{\psi_j\}_{j=1}^{r_p}$ , which span the reduced spaces  $\mathbb{U}^{r_u}$  and  $\mathbb{Q}^{r_p}$ . We can expand  $u_{r_u} \in \mathbb{U}^{r_u}$  and  $p_{r_p} \in \mathbb{Q}^{r_p}$  as

$$(3) \quad u_{r_u} \doteq u^{r_u}(x, t) = \sum_{j=1}^r a_j^u(t) \phi_j(x) \quad \text{and} \quad p_{r_p} \doteq p^{r_p}(x, t) = \sum_{j=1}^r a_j^p(t) \psi_j(x),$$

where we denote the reduced coefficients as  $\{a_j^u(t)\}_{j=1}^{r_u}$  and  $\{a_j^p(t)\}_{j=1}^{r_p}$  [54]. The bases are built from the snapshots  $\{u_i\}_{i=1}^{N_{\max}} \subseteq \{u^k\}_{k=1}^{N_T}$  and  $\{p_i\}_{i=1}^{N_{\max}} \subseteq \{p^k\}_{k=1}^{N_T}$ , where  $N_{\max}$  is the number of snapshots we consider. Here, for the sake of simplicity, we assume that  $N_{\max}$  is the same for velocity and pressure, but, in principle, the velocity and pressure snapshots number may not coincide. In our setting, the snapshots are obtained from a regularized model, since the EFR approach is applied at the FOM level as described in section 2. Next, we outline the proper orthogonal decomposition (POD) algorithm [7, 16, 38] that we use to build the reduced spaces. First, we stress that we apply *supremizer stabilization* to enrich  $\mathbb{U}^r$  and guarantee the well-posedness of the reduced system [7, 64]. The supremizer stabilization avoids spurious reduced pressure modes. We note that, when dealing with convection dominated setting, other stabilization strategies are needed at the reduced level; we postpone this topic to sections 2.4 and appendix A. We define the supremizer operator  $S : \mathbb{Q}^{N_h^p} \rightarrow \mathbb{U}^{N_h^u}$  as

$$(4) \quad (S(p), \tau)_{\mathbb{U}} = (p, \nabla \cdot \tau), \quad \forall \tau \in \mathbb{U}^{N_h^u}.$$

The enriched reduced velocity space is

$$(5) \quad \mathbb{U}^{r_{us}} \doteq \text{POD}(\{u_i\}_{i=1}^{N_{\max}}, r_u) \oplus \text{POD}(\{S(p_i)\}_{i=1}^{N_{\max}}, r_s).$$

For the pressure, we employ the standard POD procedure

$$\mathbb{Q}^{r_p} \doteq \text{POD}(\{p_i\}_{i=1}^{N_p}, r_p).$$

From these processes, we retain  $r_u$ ,  $r_s$ , and  $r_p$  modes for velocity, supremizer, and pressure, respectively, where the enriched velocity space has  $r_{us} = r_u + r_s$  modes. Thus, the bases are of the form  $\{\phi_j\}_{j=1}^{r_{us}}$  and  $\{\psi_j\}_{j=1}^{r_p}$ , for the velocity and pressure, respectively. After building the bases, for each time instance  $t^{n+1}$ , we project the system onto this low-dimensional space, solving the weak formulation of the NSE:

$$(6) \quad \begin{cases} \int_{\Omega} \frac{u_{r_{us}}^{n+1} - u_{r_{us}}^n}{\Delta t} \cdot \phi_i \, dx + \nu a(u_{r_{us}}^{n+1}, \phi_i) + c(u_{r_{us}}^{n+1}; u_{r_{us}}^{n+1}, \phi_i) - b(\phi_i, p_{r_p}^{n+1}) = 0, \\ b(u_{r_{us}}^{n+1}, \psi_j) = 0, \end{cases}$$

for all  $i = 1, \dots, r_{us}$ , and  $j = 1, \dots, r_p$ , where

$$\begin{aligned} a(u, v) &= \int_{\Omega} \nabla u : \nabla v \, dx && \forall u, v \in \mathbb{U}, \\ b(v, p) &= \int_{\Omega} p \nabla \cdot v \, dx && \forall p \in \mathbb{Q} \text{ and } \forall v \in \mathbb{U}, \\ c(w; u, v) &= \int_{\Omega} (w \cdot \nabla) u \cdot v \, dx && \forall w, u, v \in \mathbb{U}. \end{aligned}$$

Following the terminology in [71], we call the resulting ROM, which is based on standard Galerkin projection onto POD spaces, as EFR-noEFR ROMs, to highlight that EFR is applied at the FOM level (to generate the snapshots), but no EFR stabilization is performed at the reduced level.

**2.4. EFR-EFR approach.** The EFR-EFR strategy employs the EFR algorithm at both the FOM and the ROM levels. While the reduced spaces are built in the same way as in section 2.3, the reduced system is different. Indeed, the EFR strategy is applied also in the reduced setting:

$$(I)_r \quad \begin{cases} \int_{\Omega} \frac{\tilde{u}_{r_{us}}^{n+1} - u_{r_{us}}^n}{\Delta t} \cdot \phi_i \, dx + \nu a(\tilde{u}_{r_{us}}^{n+1}, \phi_i) + c(\tilde{u}_{r_{us}}^{n+1}; \tilde{u}_{r_{us}}^{n+1}, \phi_i) - b(\phi_i, p_{r_p}^{n+1}) = 0, \\ b(\tilde{u}_{r_{us}}^{n+1}, \psi_j) = 0, \end{cases}$$

$$(II)_r \quad \delta^2 a(\bar{u}_{r_{us}}^{n+1}, \phi_i) + \int_{\Omega} \bar{u}_{r_{us}}^{n+1} \cdot \phi_i \, dx = \int_{\Omega} \tilde{u}_{r_{us}}^{n+1} \cdot \phi_i \, dx,$$

$$(III)_r \quad u_{r_{us}}^{n+1} = (1 - \chi) \tilde{u}_{r_{us}}^{n+1} + \chi \bar{u}_{r_{us}}^{n+1}.$$

The reduced variables  $\bar{u}_{r_{us}}$  and  $\tilde{u}_{r_{us}}$  can be expressed in  $\mathbb{U}^r$  as

$$(7) \quad \bar{u}_{r_{us}} \doteq \bar{u}_{r_{us}}(x, t) = \sum_{j=1}^{r_{us}} a_j^{\bar{u}}(t) \phi_j(x) \quad \text{and} \quad \tilde{u}_{r_{us}} \doteq \tilde{u}_{r_{us}}(x, t) = \sum_{j=1}^{r_{us}} a_j^{\tilde{u}}(t) \phi_j(x).$$

The use of the EFR-EFR strategy is beneficial when dealing with large Reynolds numbers, since it alleviates numerical oscillations that often arise at the ROM level in the convection-dominated regime. This is illustrated numerically in Appendix A.

### 3. A NEW FEEDBACK CONTROL STRATEGY FOR HIGH REYNOLDS NUMBERS

In this section, we propose a novel feedback control strategy for high Reynolds numbers. In section 3.1, we present the new control strategy for the continuous case, and in section 3.2, we present it for the discrete case.

**3.1. Continuous formulation.** Let  $u \in \mathbb{U}$  and  $p \in \mathbb{Q}$  be the state velocity and pressure variables. Moreover, let  $f \in L^2((0, T); L^2(\Omega))$  be the distributed control. The action of  $f$  steers  $u$  toward a target divergence-free velocity  $U$ . The three variables verify the weak formulation of the NSE almost everywhere for  $t \in (0, T)$ :

$$(8) \quad \begin{cases} \langle u_t, v \rangle + \nu a(u, v) + c(u; u, v) + b(v, p) = \langle f, v \rangle & \forall v \in H_{\Gamma_D}^1(\Omega), \\ b(u, q) = 0 & \forall q \in L^2(\Omega), \end{cases}$$

where the forms are the ones introduced in section 2.3. The problem features Dirichlet and Neumann boundary conditions, and an initial velocity  $u_0$ . We leverage the control to reach the following goal:

$$(9) \quad \frac{d}{dt} \|u - U\|_{L^2}^2 \leq 0 \quad \text{a.e. in } (0, T).$$

Namely, we want the solution, in time, to become more and more similar to the desired state  $U$ . This goal (9) is achieved by using a linear feedback control in the first variable  $u$ , i.e., by appropriately choosing  $f = f(u, U)$ . If (9) holds for a solution of (8), then  $(u, p, f)$  is an *admissible solution*.

We consider a divergence-free vector field  $U$  in the following space [33]:

$$\mathcal{U}_d = \{U : U \in C((0, T), H_{u_D}^1(\Omega) \cap H^2(\Omega)) \text{ and } U_t \in C((0, T), H^1(\Omega))\}.$$

In our setting, the desired state  $U$  features the same Dirichlet boundary condition as the velocity field  $u$ . The force associated to  $U$  is defined as

$$(10) \quad F = U_t - \nu \Delta U + (U \cdot \nabla)U.$$

We stress that we deal with a desired state that asymptotically reaches a steady state  $\hat{U}$ . Thus, for every  $\epsilon > 0$  there exists  $\hat{t} > 0$  such that  $|U_t| \leq \epsilon$ .

We aim at building a linear feedback control law to deal with high  $Re$  values. First, we recall two inequalities that will be used in what follows [60]:

- *Poincaré inequality*:  $\|u\|_{L^2}^2 \leq C_P \|\nabla u\|_{L^2}^2$ , for all  $u \in H_0^1(\Omega)$ ,
- *continuity of  $c(\cdot; \cdot, \cdot)$* :  $c(u; w, v) \leq K_0 \|\nabla u\|_{L^2} \|\nabla w\|_{L^2} \|\nabla v\|_{L^2}$  for all  $u, w, v \in H^1(\Omega)$ .

We denote the inverse of the Poincaré constant with  $C_0 = C_P^{-1}$  and the continuity constant of  $c(\cdot; \cdot, \cdot)$  with  $K_0$ . To build the linear feedback law, we draw inspiration from [33], where the following theorem is stated for homogeneous boundary conditions over the whole boundary  $\partial\Omega$ :

**Theorem 1.** [33, Theorem 1] *Let  $f_A = f(u, U) = F - \gamma(u - U)$  be the chosen linear feedback control law with  $\gamma > M = \max\{0, -C_0(\nu - K_0\|U\|_{L^\infty((0, T); H^1(\Omega))})\}$ . Assuming  $(\nu - K_0\|U\|_{L^\infty((0, T); H^1(\Omega))}) > 0$  and  $u|_{\partial\Omega} = U|_{\partial\Omega} = 0$ ,*

- (i) *if  $(u, p, f_A)$  is a solution to (8), then the solution is admissible, i.e., (9) holds,*
- (ii) *and*

$$\|u(t) - U(t)\|_{L^2}^2 \leq \|u_0 - U_0\|_{L^2}^2 e^{-2(\gamma - M)t} \quad \text{a.e. } t \in (0, T),$$

*i.e., the convergence is exponential.*

**Remark 1.** *We stress that, in Theorem 1, the assumption*

*$(\nu - K_0\|U\|_{L^\infty((0, T); H^1(\Omega))}) > 0$  is essential to reach both (i) and (ii). Indeed, the hypothesis  $(\nu - K_0\|U\|_{L^\infty((0, T); H^1(\Omega))}) > 0$  is exploited to make use of a Poincaré's inequality necessary to prove the exponential convergence. The interested reader may refer to the original paper for the proof.*

*In our high  $Re$  setting, where small values of  $\nu$  are investigated, Theorem 1 does not always hold. To overcome this issue, in the novel Theorem 2, we propose an important practical extension of the results in [33], putting forth a new definition for the control  $f$  to deal with convection-dominated problems (i.e., higher  $Re$ ) and the presence of mixed boundary conditions.*

**Theorem 2.** *Let  $f_B = f(u, U) = F + (u - U)\nabla U - \gamma(u - U)$  be a linear feedback control law with  $\gamma \geq 0$ . Assuming  $u|_{\Gamma_D} = U|_{\Gamma_D}$  and  $(u \cdot n) \geq 0$  on  $\Gamma_N$ ,*

- (i) *if  $(u, p, f_B)$  is a solution to (8), then the solution is admissible, i.e., (9) holds,*

(ii) and

$$\|u(t) - U(t)\|_{L^2}^2 \leq \|u_0 - U_0\|_{L^2}^2 e^{-2(\gamma + C_0\nu)t} \quad \text{a.e. } t \in (0, T),$$

i.e., the convergence is exponential.

**Remark 2.** We emphasize that Theorem 2 does not have any restrictions on the kinematic viscosity  $\nu$ , i.e., does not depend on the Reynolds number. Furthermore, it does not depend on the Dirichlet boundary condition  $\Gamma_D$  either. In contrast, Theorem 1 holds only for large  $\nu$  values (which satisfy the constraint in Theorem 1) and for homogeneous Dirichlet conditions all over the boundary, i.e.,  $\Gamma_D = \partial\Omega$ . Thus, the new control in Theorem 2 fundamentally changes the nature of  $f$  in Theorem 1 to deal with larger Reynolds numbers, as we will show in the numerical results of section 5.2.

*Proof.* First, we define  $w = u - U$ . We want to estimate the term

$$\frac{d}{dt} \|u - U\|_{L^2}^2 = \frac{d}{dt} \|w\|_{L^2}^2.$$

We add  $\pm \langle U_t, v \rangle$ ,  $\pm \nu a(U, v)$ ,  $\pm c(U; U, v)$  to the left-hand side of the momentum equation of (8) and obtain

$$\begin{aligned} \langle w_t, v \rangle + \nu a(w, v) + \underbrace{c(u; u, v) - c(U; U, v)}_{c(w; w, v) + c(w; U, v) + c(U; w, v)} + b(v, p) \\ + \underbrace{\langle U_t, v \rangle + \nu a(U, v) + c(U; U, v)}_{\langle F, v \rangle, \text{ see (10)}} = \langle f, v \rangle \quad \forall v \in H_0^1(\Omega). \end{aligned}$$

We choose  $v = w$  and obtain, thanks to the divergence-free property of  $w$ ,

$$(11) \quad \langle w_t, w \rangle + \nu a(w, w) + c(w; w, w) + c(w; U, w) + c(U; w, w) - \langle f - F, w \rangle = 0.$$

We note that

$$(12) \quad c(w; w, w) = \frac{1}{2} \int_{\Gamma_D \cup \Gamma_N} w^2 (w \cdot n) \, dx \quad \text{and} \quad c(U; w, w) = \frac{1}{2} \int_{\Gamma_D \cup \Gamma_N} w^2 (U \cdot n) \, dx.$$

Using  $w \in H_{\Gamma_D}^1(\Omega)$  and the outflow boundary condition, we have

$$(13) \quad c(w; w, w) + c(U; w, w) = \frac{1}{2} \int_{\Gamma_N} w^2 (u \cdot n) \, dx \geq 0.$$

Moreover, choosing  $f = f_B$ , we obtain

$$(14) \quad \langle f, w \rangle = \langle F, w \rangle + c(w; U, w) - \gamma \|w\|_{L^2}^2.$$

Plugging (14) into (11), applying Poincaré's inequality to  $\nu a(w, w)$ , using inequality (13), and noticing that

$$\langle w_t, w \rangle = \frac{1}{2} \frac{d}{dt} \|w\|_{L^2}^2,$$

we obtain

$$(15) \quad \frac{1}{2} \frac{d}{dt} \|w\|_{L^2}^2 + \nu C_0 \|w\|_{L^2}^2 + \gamma \|w\|_{L^2}^2 \leq 0,$$

that is,

$$(16) \quad \frac{1}{2} \frac{d}{dt} \|w\|_{L^2}^2 \leq -(\gamma + \nu C_0) \|w\|_{L^2}^2 < 0.$$

Thus, we proved (i). Thesis (ii) is a consequence of Gronwall's inequality, which yields

$$\|u(t) - U(t)\|_{L^2}^2 \leq \|u_0 - U_0\|_{L^2}^2 e^{-2(\gamma + \nu C_0)t} \quad \text{a.e. } t \in (0, T).$$

□

**Remark 3.** We stress that the assumption of  $(u \cdot n) \geq 0$  on  $\Gamma_D$  does not allow backflow on the Neumann boundary. This assumption might be restrictive in some settings and real-life scenarios. The hypothesis can be removed if

- we assume Dirichlet conditions over the whole boundary and  $u|_{\partial\Omega} = U|_{\partial\Omega}$  or

◦ we define a nonlinear control law  $\tilde{f}_B$  that, in weak form, reads as follows: for all  $v \in H_{\Gamma_D}^1(\Omega)$ ,

$$\langle \tilde{f}_B, v \rangle = \langle f_B, v \rangle + \int_{\Gamma_N} (u - U)(u \cdot n)v \, dx.$$

We also emphasize that the outflow assumption is not needed at the discrete level (see Theorem 4).

**3.2. Discrete formulation.** In this section, we extend the novel feedback control strategy for high Reynolds numbers from the continuous setting (see section 3.1) to the discrete setting. To this end, we use the same framework as that employed for the uncontrolled problem in section 2. Specifically, we use a  $\mathbb{P}^2 - \mathbb{P}^1$  Taylor-Hood spatial discretization and the implicit Euler time discretization, which yields the following system:

$$(17) \quad \begin{cases} \int_{\Omega} \frac{u^{n+1} - u^n}{\Delta t} \cdot v_h \, dx + \nu a(u^{n+1}, v_h) + \tilde{c}(u^{n+1}; u^{n+1}, v_h) \\ -b(v_n, p^{n+1}) = \int_{\Omega} f^{n+1}(u^{n+1}, U^n, U^{n+1}) \cdot v_h \, dx & \forall v_h \in \mathbb{U}_h^{N_h^u}, \\ b(u^{n+1}, q_h) = 0, & \forall q_h \in \mathbb{Q}_h^{N_h^p}, \end{cases}$$

where  $\tilde{c}(\cdot; \cdot, \cdot)$  is the skew-symmetric approximation of the form  $c(\cdot; \cdot, \cdot)$  (see [46, 73]) defined as

$$(18) \quad \tilde{c}(u; v, z) = \frac{1}{2}[c(u; v, z) - c(u; z, v)] \quad \forall u, v, z \in U^{N_h^u}.$$

We recall that the superscript  $n$  denotes a variable evaluated at the time  $t^n$ . We note that the discrete control  $f^{n+1}$  depends on the velocity variable at time  $t^{n+1}$  and on the desired profile at times  $t^n$  and  $t^{n+1}$ . Indeed, the new control law we propose is related to the forcing term  $F$  introduced in (10). In the fully-discrete setting, we approximate  $F$  as follows:

$$(19) \quad F^{n+1} = \frac{U^{n+1} - U^n}{\Delta t} + \nu \Delta U^{n+1} + (U^{n+1} \cdot \nabla) U^{n+1}.$$

We recall that  $U$  is taken divergence-free at each time instance, which implies that  $b(U^{n+1}, q_h) = 0$  for all  $q_h \in \mathbb{Q}_h^{N_h^p}$  and  $n = 0, \dots, N_T$ . In the fully-discrete framework, the definition of *admissible solution* translates into

$$(20) \quad \|u^{n+1} - U^{n+1}\|_{L^2}^2 \leq \|u^n - U^n\|_{L^2}^2 \quad \text{for } n = 0, \dots, N_T - 1.$$

In this setting, the following theorem is proved in [33]:

**Theorem 3.** [33, Theorem 3] *Let  $f_A^{n+1} = f^{n+1}(u^{n+1}, U^n, U^{n+1}) = F^{n+1} - \gamma(u^{n+1} - U^{n+1})$  be the chosen linear feedback control law with  $\gamma > M = \max\{0, -C_0(\nu - K_0\|U\|_{L^\infty((0,T);H^1(\Omega))})\}$ . Assuming  $(\nu - K_0\|U\|_{L^\infty((0,T);H^1(\Omega))}) > 0$  and  $u|_{\partial\Omega} = U|_{\partial\Omega} = 0$ ,*

- (i) *if  $(u^{n+1}, p^{n+1}, f_A^{n+1})$  is a solution to (17), then the solution is admissible, i.e., (20) holds,*
- (ii) *and*

$$\|u^{n+1} - U^{n+1}\|^2 \leq \left( \frac{1}{1 + 2\Delta t(\gamma + C_0(\nu - K_0\|U\|_{L^\infty((0,T);H^1(\Omega))})} \right)^{n+1} \|u_0^h - U_0^h\|^2.$$

In the novel Theorem 4, we generalize Theorem 3 to cases where  $(\nu - K_0\|U\|_{L^\infty((0,T);H^1(\Omega))})$  can be negative, i.e., to the case  $\nu \ll 1$ , which is generally the case of interest in realistic settings. Before stating the theorem, we define the weak form of the control  $f_B$  at time  $t^{n+1}$  as

$$(21) \quad \langle f_B^{n+1}, v \rangle = \langle F_B^{n+1}, v \rangle + \tilde{c}(u^{n+1} - U^{n+1}; U^{n+1}, v) - \gamma \langle u^{n+1} - U^{n+1}, v \rangle,$$

for all  $v \in H_{\Gamma_D}^1(\Omega)$ , where

$$(22) \quad \langle F_B^{n+1}, v \rangle = \int_{\Omega} \frac{U^{n+1} - U^n}{\Delta t} v \, dx + \nu a(U^{n+1}, v) + \tilde{c}(U^{n+1}; U^{n+1}, v).$$

**Theorem 4.** *Let  $f_B^{n+1}$  be the novel linear feedback control law defined in (21) with  $\gamma \geq 0$  and  $u|_{\Gamma_D} = U|_{\Gamma_D}$ .*

- (i) *If  $(u^{n+1}, p^{n+1}, f_B^{n+1})$  is a solution to (17), then the solution is admissible, i.e., (20) holds,*



(ii) and

$$\|u^{n+1} - U^{n+1}\|_{L^2}^2 \leq \left( \frac{1}{1 + 2\Delta t(\gamma + C_0\nu)} \right)^{n+1} \|u_0^h - U_0^h\|_{L^2}^2.$$

*Proof.* For the sake of notation, we define  $w^{n+1} = u^{n+1} - U^{n+1}$ . Notice that, thanks to the assumption  $u|_{\Gamma_D} = U|_{\Gamma_D}$ ,  $w^{n+1} \in \mathbb{U}^{N_h^n} \subset H_{\Gamma_D}^1(\Omega)$ . We want to bound the term  $\|w^{n+1}\|_{L^2}$  with  $\|w^n\|_{L^2}$ . To this end, we add the following terms to the left-hand side of the momentum equation of (17):

$$(23) \quad \pm \int_{\Omega} \frac{U^{n+1}}{\Delta t} v_h \, dx, \quad \pm \int_{\Omega} \frac{U^n}{\Delta t} v_h \, dx, \quad \pm \nu a(U^{n+1}, v_h), \quad \text{and} \quad \pm \tilde{c}(U^{n+1}; U^{n+1}, v_h).$$

Recalling that  $w^{n+1} = u^{n+1} - U^{n+1}$ , we obtain

$$(24) \quad \int_{\Omega} \frac{w^{n+1} - w^n}{\Delta t} v_h \, dx + \nu a(w^{n+1}, v_h) + \underbrace{\tilde{c}(u^{n+1}; u^{n+1}, v_h) - \tilde{c}(U^{n+1}; U^{n+1}, v_h)}_{\tilde{c}(w^{n+1}; w^{n+1}, v_h) + \tilde{c}(w^{n+1}; U^{n+1}, v_h) + \tilde{c}(U^{n+1}; w^{n+1}, v_h)} \\ + b(v_h, p^n) + \underbrace{\int_{\Omega} \frac{U^{n+1} - U^n}{\Delta t} v_h \, dx + \nu a(U^{n+1}, v_h) + \tilde{c}(U^{n+1}; U^{n+1}, v_h)}_{\langle F^{n+1}, v_h \rangle \text{ see (22)}} = \int_{\Omega} f^{n+1} v_h \, dx.$$

Let us choose  $v_h = w^{n+1}$ . Since  $\tilde{c}(\cdot; \cdot, \cdot)$  is skew-symmetric, we have  $\tilde{c}(u; v, v) = 0$  for every  $u, v$  in  $\mathbb{U}^{N_h^n}$ . Moreover, notice that  $w^{n+1}$  is divergence-free as the difference of two divergence-free functions. Then, equation (24) becomes

$$(25) \quad \int_{\Omega} \frac{w^{n+1} - w^n}{\Delta t} w_{n+1} \, dx + \nu a(w^{n+1}, w^{n+1}) \\ + \tilde{c}(w^{n+1}; U^{n+1}, w^{n+1}) - \int_{\Omega} (f^{n+1} - F^{n+1}) w^{n+1} \, dx = 0.$$

Choosing  $\int_{\Omega} f^{n+1} v_h \, dx = \langle f^{n+1}, v_h \rangle = \langle f_B^{n+1}, v_h \rangle$  in (17), we obtain

$$(26) \quad \int_{\Omega} f^{n+1} w^{n+1} \, dx = \langle F^{n+1}, w^{n+1} \rangle + \tilde{c}(w^{n+1}; U^{n+1}, w^{n+1}) - \gamma \|w^{n+1}\|_{L^2}^2.$$

Plugging (26) into (25), applying Poincaré's inequality to  $\nu a(w^{n+1}, w^{n+1})$ , and noticing that

$$\int_{\Omega} \frac{w^{n+1} - w^n}{\Delta t} \cdot w^{n+1} \, dx = \frac{1}{2\Delta t} \|w^{n+1}\|_{L^2}^2 + \frac{1}{2\Delta t} \|w^{n+1} - w^n\|_{L^2}^2 - \frac{1}{2\Delta t} \|w^n\|_{L^2}^2,$$

we have

$$\frac{1}{2\Delta t} \|w^{n+1}\|_{L^2}^2 + \frac{1}{2\Delta t} \|w^{n+1} - w^n\|_{L^2}^2 + \nu C_0 \|w^{n+1}\|_{L^2}^2 + \gamma \|w^{n+1}\|_{L^2}^2 \leq \frac{1}{2\Delta t} \|w^n\|_{L^2}^2.$$

Since  $\|w^{n+1} - w^n\|_{L^2}^2 \geq 0$ , we obtain

$$(27) \quad \|w^{n+1}\|_{L^2}^2 \leq \left( \frac{1}{1 + 2\Delta t(\gamma + C_0\nu)} \right) \|w^n\|_{L^2}^2,$$

which proves (i). Thesis (ii) is obtained applying inequality (27) recursively.  $\square$

**Remark 4** (The role of  $\gamma$ ). *In the controlled setting, the parameter  $\gamma$  represents a penalization parameter with respect to the control action. A large value of  $\gamma$  allows a faster convergence towards the desired state. However, in real applications, a large value of  $\gamma$  translates into a large physical and economic effort in controlling the system. Since one wants to spend as few resources as possible to reach the goal, we investigate the cases where  $\gamma \rightarrow 0$  and how this affects the convergence rate. Moreover, we stress that, since we are working with large  $Re$ ,  $\gamma \rightarrow 0$  translates into a system that may feature numerical instabilities, which may require further stabilization besides the control action. This feature has already been observed in the optimal control framework for convection-dominated advection-diffusion equations, see, e.g., [76, 77].*

## 4. EFR STABILIZATION FOR THE NEW FEEDBACK CONTROL

As explained in Remark 4, when  $\gamma \rightarrow 0$ , further stabilization may be needed in addition to the control stabilizing effect. In this section, we leverage the EFR strategy to stabilize the novel feedback control introduced in section 3 in the convection-dominated setting (i.e., for large Reynolds numbers). Specifically, in section 4.1, we outline and analyze the new feedback control strategy with EFR stabilization at the FOM level. In section 4.2, we propose a new adaptive EFR strategy to improve the accuracy of the feedback control at the FOM level. Finally, we compare the feedback control without (section 4.3) and with (section 4.4) EFR stabilization at the ROM level.

**4.1. EFR algorithm.** The EFR strategy for the control case is similar to the EFR strategy for the uncontrolled case. The main difference is the presence of  $f^{n+1}(\tilde{u}^{n+1}, U^n, U^{n+1})$  on the right-hand side of the evolve step. Indeed, using the implicit Euler method for the time discretization with the relaxation parameter  $\chi \in [0, 1]$ , the EFR approach for the controlled system at the time  $t^{n+1}$  reads:

$$\begin{aligned}
\text{(I)}_c \quad \text{Evolve:} \quad & \begin{cases} \frac{\tilde{u}^{n+1} - u^n}{\Delta t} + (\tilde{u}^{n+1} \cdot \nabla) \tilde{u}^{n+1} & \\ -\nu \Delta \tilde{u}^{n+1} + \nabla p^{n+1} = f^{n+1}(\tilde{u}^{n+1}, U^n, U^{n+1}) & \text{in } \Omega, \\ \nabla \cdot \tilde{u}^{n+1} = 0 & \text{in } \Omega, \\ \tilde{u}^{n+1} = u_D^{n+1} & \text{on } \Gamma_D, \\ -p^{n+1} n + \frac{\partial \tilde{u}^{n+1}}{\partial n} = 0 & \text{on } \Gamma_N. \end{cases} \\
\text{(II)}_c \quad \text{Filter:} \quad & \begin{cases} -\delta^2 \Delta \bar{u}^{n+1} + \bar{u}^{n+1} = \tilde{u}^{n+1} & \text{in } \Omega, \\ \bar{u}^{n+1} = u_D^{n+1} & \text{on } \Gamma_D, \\ \frac{\partial \bar{u}^{n+1}}{\partial n} = 0 & \text{on } \Gamma_N. \end{cases} \\
\text{(III)}_c \quad \text{Relax:} \quad & u^{n+1} = (1 - \chi) \tilde{u}^{n+1} + \chi \bar{u}^{n+1}.
\end{aligned}$$

The only difference from the uncontrolled setting is in step (I), since only there the control action is present. Next, we prove a convergence result for the new feedback control strategy with EFR stabilization, which is outlined in steps (I)<sub>c</sub>–(III)<sub>c</sub>.

**Theorem 5.** *Let  $f_B^{n+1} = f^{n+1}(\tilde{u}^{n+1}, U^n, U^{n+1}) = F^{n+1} + (\tilde{u}^{n+1} - U^{n+1}) \nabla U^{n+1} - \gamma(\tilde{u}^{n+1} - U^{n+1})$  be the chosen linear feedback control law with  $\gamma \geq 0$ ,  $0 < \chi < 1$ ,  $\bar{C}(\tilde{u}^k) = C(\delta h_{max}^2 + h_{max}^3 + \delta^2 \|\Delta \tilde{u}^k\|_{L^2})$  for some positive constant  $C$  and  $k = 0, \dots, n+1$ . We assume that  $\tilde{u}|_{\Gamma_D} = U|_{\Gamma_D}$ . If  $(\tilde{u}^{n+1}, p^{n+1}, f_B^{n+1})$  is a solution to step (I)<sub>c</sub> and  $u^{n+1}$  is the EFR velocity defined in (III)<sub>c</sub>, then, for any  $0 < \varepsilon < 1$ , the following holds:*

$$\begin{aligned}
\|u^{n+1} - U^{n+1}\|_{L^2}^2 &\leq \left( \frac{1}{(1 - \varepsilon)(1 + 2\Delta t(\gamma + C_0\nu))} \right)^{n+1} \|u_0^h - U_0^h\|_{L^2}^2 \\
&+ \frac{\chi^2}{\varepsilon(1 - \varepsilon)(1 + 2\Delta t(\gamma + C_0\nu))} \sum_{i=1}^n \bar{C}(\tilde{u}^i)^2 + \frac{\chi^2 \bar{C}(\tilde{u}^{n+1})^2}{\varepsilon}.
\end{aligned} \tag{28}$$

*Proof.* We define the variables  $\tilde{w}^{n+1} = \tilde{u}^{n+1} - U^{n+1}$  and  $w^n = u^n - U^n$ . Both variables are in  $H_{\Gamma_D}^1(\Omega)$ . The proof is analogous to the proof of Theorem 4. Indeed, we add the quantities in (23) to the left-hand side of the evolve step in (I)<sub>c</sub>. Choosing  $v_h = \tilde{w}^{n+1}$  and using the definition of  $f_B$ , we obtain the relation

$$\|\tilde{w}^{n+1}\|_{L^2}^2 \leq \left( \frac{1}{1 + 2\Delta t(\gamma + C_0\nu)} \right) \|w^n\|_{L^2}^2. \tag{29}$$

It remains to prove that  $\|\tilde{w}^{n+1}\|_{L^2}^2 \geq C_1 \|w^{n+1}\|_{L^2}^2 - C_2$ , for some  $C_1 > 0$  and  $C_2 \geq 0$ . We start with the relax step of the EFR algorithm

$$(30) \quad u^{n+1} = (1 - \chi) \tilde{u}^{n+1} + \chi \bar{u}^{n+1}$$

and subtract  $U^{n+1}$  from both sides:

$$\begin{aligned} w^{n+1} &= u^{n+1} - U^{n+1} = (1 - \chi) \tilde{u}^{n+1} + \chi \bar{u}^{n+1} - (1 - \chi) U^{n+1} - \chi U^{n+1} \\ &= (1 - \chi) \tilde{w}^{n+1} + \chi (\bar{u}^{n+1} - U^{n+1}) \\ &= (1 - \chi) \tilde{w}^{n+1} + \chi (\bar{u}^{n+1} - \tilde{u}^{n+1}) + \chi (\tilde{u}^{n+1} - U^{n+1}) \\ &= (1 - \chi) \tilde{w}^{n+1} + \chi (\bar{u}^{n+1} - \tilde{u}^{n+1}) + \chi \tilde{w}^{n+1} \\ &= \tilde{w}^{n+1} + \chi (\bar{u}^{n+1} - \tilde{u}^{n+1}). \end{aligned}$$

By the triangle inequality and by Lemma 2.12 in [45], we obtain, for some positive constant  $C$ ,

$$(31) \quad \|w^{n+1}\|_{L^2} \leq \|\tilde{w}^{n+1}\|_{L^2} + \chi \|\bar{u}^{n+1} - \tilde{u}^{n+1}\|_{L^2} \leq \|\tilde{w}^{n+1}\|_{L^2} + \chi C (\delta h_{max}^2 + h_{max}^3 + \delta^2 \|\Delta \tilde{u}^{n+1}\|_{L^2}).$$

For the sake of clarity, let us define  $\bar{C}(\tilde{u}^{n+1}) = C(\delta h_{max}^2 + h_{max}^3 + \delta^2 \|\Delta \tilde{u}^{n+1}\|_{L^2})$ . Inequality (31) implies, exploiting Young's inequality with  $0 < \varepsilon < 1$ ,

$$\begin{aligned} \|\tilde{w}^{n+1}\|_{L^2}^2 &\geq (\|w^{n+1}\|_{L^2} - \chi \bar{C}(\tilde{u}^{n+1}))^2 = \|w^{n+1}\|_{L^2}^2 + \chi^2 \bar{C}(\tilde{u}^{n+1})^2 - 2\chi \bar{C}(\tilde{u}^{n+1}) \|w^{n+1}\|_{L^2} \\ &\geq \|w^{n+1}\|_{L^2}^2 + \chi^2 \bar{C}(\tilde{u}^{n+1})^2 - \|w^{n+1}\|_{L^2}^2 \varepsilon - \frac{\chi^2 \bar{C}(\tilde{u}^{n+1})^2}{\varepsilon} \\ &= (1 - \varepsilon) \left( \|w^{n+1}\|_{L^2}^2 - \frac{\chi^2 \bar{C}(\tilde{u}^{n+1})^2}{\varepsilon} \right). \end{aligned}$$

Exploiting this relation in (29), we obtain

$$(32) \quad \|w^{n+1}\|_{L^2}^2 \leq \left( \frac{1}{(1 - \varepsilon)(1 + 2\Delta t(\gamma + C_0\nu))} \right) \|w^n\|_{L^2}^2 + \frac{\chi^2 \bar{C}(\tilde{u}^{n+1})^2}{\varepsilon}.$$

Applying (32) to  $w^n$ , we have

$$\begin{aligned} \|w^{n+1}\|_{L^2}^2 &\leq \left( \frac{1}{(1 - \varepsilon)(1 + 2\Delta t(\gamma + C_0\nu))} \right)^2 \|w^{n-1}\|_{L^2}^2 \\ &\quad + \frac{\chi^2 \bar{C}(\tilde{u}^n)^2}{\varepsilon(1 - \varepsilon)(1 + 2\Delta t(\gamma + C_0\nu))} + \frac{\chi^2 \bar{C}(\tilde{u}^{n+1})^2}{\varepsilon}. \end{aligned}$$

Finally, applying relation (32) recursively, we obtain the thesis.  $\square$

**Remark 5** (on the EFR convergence). *From Theorem 5, we observe that EFR strategy worsens the bound in Theorem 4 since no exponential convergence and admissibility are guaranteed. Next, we analyze the three terms separately.*

(1)  $\left( \frac{1}{(1 - \varepsilon)(1 + 2\Delta t(\gamma + C_0\nu))} \right)^{n+1} \|u_0^h - U_0^h\|_{L^2}^2$ : *It is clear that, for an arbitrary small  $\varepsilon$ , a small  $\gamma$ , and a large Reynolds number, this term scales as follows:*

$$\left( \frac{1}{(1 - \varepsilon)(1 + 2\Delta t(\gamma + C_0\nu))} \right)^{n+1} \|u_0^h - U_0^h\|_{L^2}^2 \sim \|u_0^h - U_0^h\|_{L^2}^2.$$

(2)  $\frac{\chi^2}{\varepsilon(1 - \varepsilon)(1 + 2\Delta t(\gamma + C_0\nu))} \sum_{i=1}^n \bar{C}(\tilde{u}^i)^2$ : *The scaling for this term is not clear, since, for  $k = 0, \dots, n$ ,  $\bar{C}(\tilde{u}^k)$  can be large. Everything depends on the scalings of the various constants and, thus, on the problem at hand.*

(3)  $\frac{\chi^2 \overline{C}(\tilde{u}^{n+1})^2}{\varepsilon}$ : The considerations for term (2) apply for this term, too.

A possible choice for  $\varepsilon$  is  $\varepsilon = \chi$ . Indeed, in our numerical frameworks  $\chi \ll 1$ . This is not a restrictive hypothesis and is a common choice in literature [15, 71], as we will explain in section 4.2. This way, the considerations for term (1) are still valid, and the following scalings for terms (2) and (3) hold:

$$(2) \sim \frac{\chi}{(1 - \chi)(1 + 2\Delta t(\gamma + C_0\nu))} \sum_{i=1}^n \overline{C}(\tilde{u}^i)^2 \sim \chi \sum_{i=1}^n \overline{C}(\tilde{u}^i)^2 \quad \text{and} \quad (3) \sim \chi \overline{C}(\tilde{u}^{n+1})^2.$$

This way, the small value of  $\chi$  can balance the possibly large values of  $\overline{C}(\tilde{u}^k)$ , for  $k = 0, \dots, n + 1$ . These observations suggest possible slow convergence or plateau phenomena even for small values of  $\chi$ , as we will see in the numerical results presented in section 5.2. We propose a solution to this issue in section 4.2.

**4.2. A new adaptive EFR (aEFR) algorithm.** The numerical investigation in section 5.2 shows that employing EFR with small relaxation parameters alleviates the spurious numerical oscillations and allows us to reach the desired state faster than noEFR in the first part of the simulation. However, as explained in Remark 5, Theorem 5 does not guarantee an exponential convergence as stated in Theorem 4 for the noEFR strategy.

This is the reason why, in this section, we propose an adaptive-EFR (aEFR) strategy, which is outlined in Algorithm 1. In the new aEFR strategy, given a tolerance  $\tau$ , we apply EFR (32) if  $\|u^n\|_{L^2} = \|u^n - U^n\|_{L^2}^2 \geq \tau$ . Otherwise, we apply the standard controlled NSE simulation (17). The main goal of the new aEFR strategy is to alleviate the oscillations in the first part of the time evolution and, when a good approximation of  $U^n$  is reached, to recover the exponential bound stated in Theorem 4. The aEFR strategy aims at tackling those settings in which, e.g., the EFR is needed in the transient regime but not for the steady state. An example of this type of setting is that used in the numerical investigation in section 5.2. We note that, although the choice of the parameter  $\tau$  in the new aEFR strategy is problem dependent, it can be guided by a threshold value for the difference between the controlled solution and the desired state. Indeed, the numerical results of section 5.2 will show that employing the new aEFR algorithm allows:

- to alleviate the numerical oscillations while there is room for improvement in reaching the desired state, and
- to recover the exponential convergence expected by Theorem 4.

---

**Algorithm 1** aEFR

---

1: $u_0, u_{in}, \tau$	▷ Inputs needed
2: <b>for</b> $n \in \{1, \dots, N_T\}$ <b>do</b>	▷ Time loop
3: <b>if</b> $\ u^n - U^n\ _{L^2}^2 \geq \tau$ <b>then</b>	
4:         (I) <sub>c</sub> + (II) <sub>c</sub> + (III) <sub>c</sub>	▷ EFR simulation
5: <b>else</b>	
6:         Solve (17)	▷ Standard controlled NSE simulation
7: <b>end if</b>	
8: <b>end for</b>	

---

**4.3. The EFR-noEFR (and aEFR-noEFR) approach.** In this section, we use the new feedback control with EFR stabilization at the FOM level, but not at the ROM level. To build the reduced bases, we apply the same POD-based ROM strategy outlined in section 2.3. Namely, we use a standard POD for the pressure variable, and a POD with supremizer enrichment technique for the velocity. The main difference is that in the EFR-noEFR approach, the snapshots are provided by the solution of the regularized control problem described in section 4.1. Also in this case, we call the reduced spaces as  $\mathbb{U}^{r_{us}}$  and  $\mathbb{Q}^{r_p}$ , which are spanned by  $\{\phi_i\}_{i=1}^{r_{us}}$  and  $\{\psi_i\}_{i=1}^{r_p}$ , respectively. After

the building phase, for each time instance  $t^{n+1}$ , a standard Galerkin projection is performed in the controlled NSE framework, i.e., we solve

$$(33) \quad \begin{cases} \int_{\Omega} \frac{u_{r_{us}}^{n+1} - u_{r_{us}}^n}{\Delta t} \phi_i dx + \nu a(u_{r_{us}}^{n+1}, \phi_i) + c(u_{r_{us}}^{n+1}; u_{r_{us}}^{n+1}, \phi_i) \\ -b(\phi_i, p_{r_p}^{n+1}) = \int_{\Omega} f^{n+1}(u_{r_{us}}^{n+1}, U^n, U^{n+1}) \phi_i dx, \\ b(u_{r_{us}}^{n+1}, \psi_j) = 0, \end{cases}$$

for all  $i = 1, \dots, r_{us}$ , and  $j = 1, \dots, r_p$ . Here,  $u_{r_{us}}$  and  $p_{r_p}$  are the reduced variables as defined in section 2.3. The strategy is summarized in Algorithm 2. We stress that an adaptive version, aEFR-noEFR, can be easily devised, as illustrated in Algorithm 3.

---

**Algorithm 2** EFR-noEFR

---

```

1:  $u_0, u_{in}, N_u, N_p$  ▷ Inputs needed
2: for  $n \in \{1, \dots, N_T\}$  do ▷ Time loop
3:   (I)c + (II)c + (III)c ▷ EFR simulation
4: end for
5:  $\{u_i\}_{i=1}^{N_u} \subseteq \{u^k\}_{k=1}^{N_T}$     $\{p_i\}_{i=1}^{N_p} \subseteq \{p^k\}_{k=1}^{N_T}$  ▷ Snapshots
6:  $\mathbb{U}^{r_{us}} \doteq \text{POD}(\{u_i\}_{i=1}^{N_u}) \oplus \text{POD}(\{S(p_i)_{i=1}^{N_u}\})$  ▷ Supremizer enrichment for velocity space
7:  $\mathbb{Q}^{r_p} \doteq \text{POD}(\{p_i\}_{i=1}^{N_p})$  ▷ Standard POD for pressure
8: for  $n \in \{1, \dots, N_T\}$  do ▷ Time loop
9:   Solve (33) ▷ Standard controlled NSE simulation
10: end for

```

---



---

**Algorithm 3** aEFR-noEFR

---

```

1:  $u_0, u_{in}, N_u, N_p, \tau$  ▷ Inputs needed
2: Apply aEFR (Algorithm 1)
3:  $\{u_i\}_{i=1}^{N_u} \subseteq \{u^k\}_{k=1}^{N_T}$     $\{p_i\}_{i=1}^{N_p} \subseteq \{p^k\}_{k=1}^{N_T}$  ▷ Snapshots
4:  $\mathbb{U}^{r_{us}} \doteq \text{POD}(\{u_i\}_{i=1}^{N_u}) \oplus \text{POD}(\{S(p_i)_{i=1}^{N_u}\})$  ▷ Supremizer enrichment for velocity space
5:  $\mathbb{Q}^{r_p} \doteq \text{POD}(\{p_i\}_{i=1}^{N_p})$  ▷ Standard POD for pressure
6: for  $n \in \{1, \dots, N_T\}$  do ▷ Time loop
7:   Solve (33) ▷ Standard controlled NSE simulation
8: end for

```

---

**4.4. EFR-EFR (and aEFR-aEFR) approach.** In this section, we use the new feedback control with EFR stabilization at both the FOM and the ROM level. The reduced spaces are built as in section 4.3. However, the Galerkin projection is performed for the three steps of the EFR as follows:

$$(I)_{cr} \quad \begin{cases} \int_{\Omega} \frac{\tilde{u}_{r_{us}}^{n+1} - u_{r_{us}}^n}{\Delta t} \phi_i dx + \nu a(\tilde{u}_{r_{us}}^{n+1}, \phi_i) + c(\tilde{u}_{r_{us}}^{n+1}; \tilde{u}_{r_{us}}^{n+1}, \phi_i) \\ -b(\phi_i, p_{r_p}^{n+1}) = \int_{\Omega} f^{n+1}(\tilde{u}_{r_{us}}^{n+1}, U^n, U^{n+1}) \phi_i dx, \\ b(\tilde{u}_{r_{us}}^{n+1}, \psi_j) = 0, \end{cases}$$

$$(II)_{cr} \quad \delta^2 a(\bar{u}_{r_{us}}^{n+1}, \phi_i) + \int_{\Omega} \bar{u}_{r_{us}}^{n+1} \phi_i dx = \int_{\Omega} \tilde{u}_{r_{us}}^{n+1} \phi_i dx,$$

$$(III)_{cr} \quad u_{r_{us}}^{n+1} = (1 - \chi) \tilde{u}_{r_{us}}^{n+1} + \chi \bar{u}_{r_{us}}^{n+1},$$

for all  $i = 1, \dots, r_{us}$ , and  $j = 1, \dots, r_p$ . As in the case of the reduced velocity  $u_{r_{us}}$  and reduced pressure  $p_{r_p}$ , the reduced variables  $\bar{u}_{r_{us}}$  and  $\tilde{u}_{r_{us}}$  are those described in section 2.4. The EFR-EFR approach is described in Algorithm 4. Also in this case, we propose the adaptive version, aEFR-aEFR, in Algorithm 5. The criterion chosen to apply or not the EFR strategy at the reduced level is  $\|\mathbf{Q}_{\mathbb{U}^{r_{us}}}^T u_r^n - U^n\| \geq \tau$ , where  $\mathbf{Q}_{\mathbb{U}^{r_{us}}}$  is the basis matrix related to the velocity space, which projects back the reduced solution to the FOM space.

For the sake of clarity, in Table 1, we summarize all the FOM and ROM acronyms and the corresponding features.

---

**Algorithm 4** EFR-EFR

---

```

1:  $u_0, u_{in}, N_u, N_p$  ▷ Inputs needed
2: for  $n \in \{1, \dots, N_T\}$  do ▷ Time loop
3:    $(\text{I})_c + (\text{II})_c + (\text{III})_c$  ▷ EFR simulation
4: end for
5:  $\{u_i\}_{i=1}^{N_u} \subseteq \{u^k\}_{k=1}^{N_T}$     $\{p_i\}_{i=1}^{N_p} \subseteq \{p^k\}_{k=1}^{N_T}$  ▷ Snapshots
6:  $\mathbb{U}^{r_{us}} \doteq \text{POD}(\{u_i\}_{i=1}^{N_u}) \oplus \text{POD}(\{S(p_i)\}_{i=1}^{N_u})$  ▷ Supremizer enrichment for velocity
7:  $\mathbb{Q}^{r_p} \doteq \text{POD}(\{p_i\}_{i=1}^{N_p})$  ▷ Standard POD for pressure
8: for  $n \in \{1, \dots, N_T\}$  do ▷ Time loop
9:    $(\text{I})_{cr} + (\text{II})_{cr} + (\text{III})_{cr}$  ▷ EFR simulation
10: end for

```

---



---

**Algorithm 5** aEFR-aEFR

---

```

1:  $u_0, u_{in}, N_u, N_p, \tau$  ▷ Inputs needed
2: Apply aEFR (Algorithm 1)
3:  $\{u_i\}_{i=1}^{N_u} \subseteq \{u^k\}_{k=1}^{N_T}$     $\{p_i\}_{i=1}^{N_p} \subseteq \{p^k\}_{k=1}^{N_T}$  ▷ Snapshots
4:  $\mathbb{U}^{r_{us}} \doteq \text{POD}(\{u_i\}_{i=1}^{N_u}) \oplus \text{POD}(\{S(p_i)\}_{i=1}^{N_u})$  ▷ Supremizer enrichment for velocity
5:  $\mathbb{Q}^{r_p} \doteq \text{POD}(\{p_i\}_{i=1}^{N_p})$  ▷ Standard POD for pressure
6: for  $n \in \{1, \dots, N_T\}$  do ▷ Time loop
7:   if  $\|\mathbf{Q}_{\mathbb{U}^{r_{us}}}^T u_r^n - U^n\|_{L^2} \geq \tau$  then
8:      $(\text{I})_{cr} + (\text{II})_{cr} + (\text{III})_{cr}$  ▷ EFR simulation
9:   else
10:    Solve (33) ▷ Standard controlled NSE simulation
11:   end if
12: end for

```

---

**Table 1.** FOM and ROM acronyms. Gray cells in ROM-columns indicate that no reduction is performed in the algorithm.

Acronym	FOM regularization	ROM regularization	FOM adaptivity	ROM adaptivity	Eq. or algorithm
noEFR					eq. (17)
EFR	✓				$(\text{I})_c + (\text{II})_c + (\text{III})_c$
aEFR	✓		✓		Algorithm 1
EFR-noEFR	✓				Algorithm 2
EFR-EFR	✓	✓			Algorithm 4
aEFR-noEFR	✓		✓		Algorithm 3
aEFR-aEFR	✓	✓	✓	✓	Algorithm 5

**Remark 6.** *No theoretical convergence study is performed at the ROM level. However, we think that it is possible to exploit the FOM results to prove a ROM version of Theorem 4 and Theorem 5, exploiting the techniques presented in [75].*

## 5. NUMERICAL RESULTS

In this section, we perform a numerical investigation of the novel feedback control and the EFR strategy used in the convection-dominated regime. To this end, in section 5.1, we compare the new feedback control strategy,  $f_B$ , with the standard control approach,  $f_A$ , in the convection-dominated regime of the NSE at the FOM level. In section 5.2, we investigate the role played by the EFR stabilization in the FOM of the convection-dominated NSE with a small control parameter  $\gamma$  (which is common in realistic applications). Finally, in section 5.3, we investigate the EFR stabilization in the ROM of the convection-dominated NSE with a small control parameter  $\gamma$ . Specifically, we perform three numerical experiments, which are summarized in Table 2:

- *Experiment 1.* A numerical comparison between the  $f_A$  and  $f_B$  control strategies in the convection-dominated regime at the FOM level, with no EFR stabilization. The goal of this experiment is to investigate whether  $f_B$  yields more accurate results than  $f_A$ .
- *Experiment 2.* A numerical comparison between noEFR, EFR, and aEFR at the FOM level with  $f_B$  control and small  $\gamma$  values. In this test, we investigate whether EFR-based strategies are useful in the controlled setting with realistic control parameter values.
- *Experiment 3.* A numerical comparison between noEFR and aEFR at the ROM level, with POD basis functions obtained from an EFR stabilized FOM. This numerical test investigates whether EFR-based strategies are beneficial at the controlled ROM level.

**Table 2.** Summary of the three numerical experiments.

	FOM	ROM	$f_A$	$f_B$	noEFR	EFR	aEFR
Experiment 1	✓		✓	✓	✓		
Experiment 2	✓			✓	✓	✓	✓
Experiment 3		✓		✓	✓		✓

### 5.1. $f_A$ vs $f_B$ Numerical Comparison for Unstabilized FOM (noEFR)(Experiment 1).

In this numerical experiment, we investigate whether the novel feedback control,  $f_B$ , yields more accurate results than the classical control approach,  $f_A$ , at the FOM level. To this end, we consider an unstabilized FOM (noEFR), and realistic, small values for the control parameter,  $\gamma$ .

The spatial domain is  $\Omega \doteq \{(0, 2.2) \times (0, 0.41)\} \setminus \{(x, y) \in \mathbb{R}^2 \text{ such that } (x - 0.2)^2 + (y - 0.2)^2 - 0.05^2 = 0\}$ , represented in Figure 1. The Dirichlet boundary condition is

$$(34) \quad u_D = \begin{cases} 0 & \text{on } \Gamma_W, \\ u_{\text{in}} = \left( \frac{6}{0.41^2} y(0.41 - y), 0 \right) & \text{on } \Gamma_{\text{in}}, \end{cases}$$

where  $\Gamma_W$  (solid teal boundary in Figure 1) is the union of the bottom ( $\Gamma_B$ ) and top ( $\Gamma_T$ ) walls of the channel together with the walls of the cylinder ( $\Gamma_C$ ). The inlet condition  $u_{\text{in}}$  is applied to  $\Gamma_{\text{in}} = \{0\} \times [0, 0.41]$ , (magenta dashed line in Figure 1). The prescribed inlet condition is given by equation (34). Moreover,  $\Gamma_N$  (black dotted boundary in Figure 1) features “free flow” boundary conditions. The initial condition is  $u_0 = (0, 0)$ . The mesh parameters of the triangular mesh (depicted in Figure 2) are  $h_{\text{min}} = 4.46 \cdot 10^{-3}$  and  $h_{\text{max}} = 4.02 \cdot 10^{-2}$ . After a Taylor-Hood  $\mathbb{P}^2 - \mathbb{P}^1$  FE discretization for velocity and pressure, respectively, we obtain a FE space with  $N_h \doteq N_h^u + N_h^p = 14053$  degrees of freedom. With these mesh parameters, as stated in [71], we are working in a marginally-resolved regime and, for high  $Re$  values, the simulation does not accurately capture the flow features, displaying numerical oscillations.

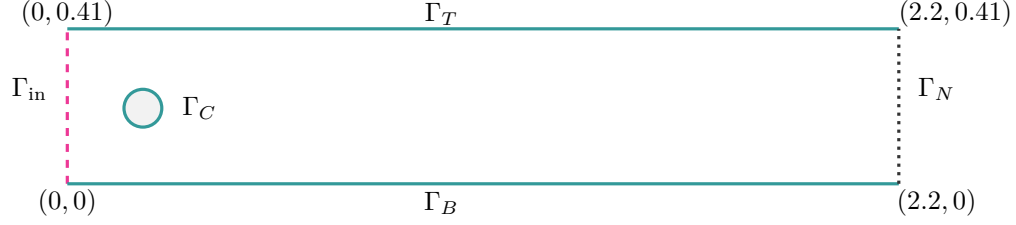


**Figure 1.** Schematic representation of the domain  $\Omega$ .  $\Gamma_D = \Gamma_{\text{in}} \cup \Gamma_C \cup \Gamma_T \cup \Gamma_B$ . No-slip conditions are applied over the teal solid boundary. The inlet condition is applied to  $\Gamma_{\text{in}}$ , i.e., the magenta dashed line. The “free flow” boundary condition is applied on  $\Gamma_N$ , i.e., the black dotted line.

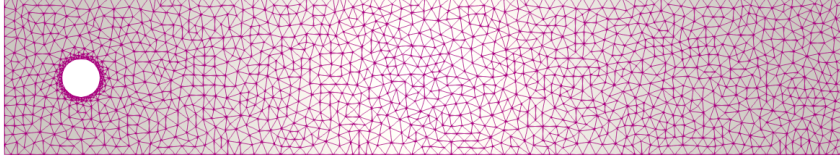


**Figure 2.** The mesh.

For example, this is the case when we set  $\nu = 10^{-4}$ ,  $T = 8$ , and  $\Delta t = 4 \cdot 10^{-4}$ . Our computational setting is similar to that in [40], although the Reynolds number used in our numerical investigation (i.e.,  $Re = 1000$ ) is one order of magnitude higher. We refer the reader to [66] for a complete description of the benchmark in an uncontrolled setting.

Our goal is to reach a desired profile  $U$  by means of the linear feedback control actions described in Theorem 1 and Theorem 4, namely  $f_A$  and  $f_B$ , respectively. We recall that, defining  $F$  as in (10),

$$f_A = F - \gamma(u - U) \quad \text{and} \quad f_B = F + (u - U)\nabla U - \gamma(u - U).$$

For the sake of clarity, we say that the system (or the velocity) is A-controlled and B-controlled when  $f_A$  and  $f_B$  are employed, respectively. In this test case, the desired velocity profile solves the following steady Stokes problem in  $\Omega$ :

$$(35) \quad \begin{cases} -\Delta U + \nabla P = 0 & \text{in } \Omega, \\ \nabla \cdot U = 0 & \text{in } \Omega, \\ U = u_D & \text{on } \Gamma_D, \\ -Pn + \frac{\partial U}{\partial n} = 0 & \text{on } \Gamma_N. \end{cases}$$

The Stokes solution, which is displayed in Figure 3, is the laminar state that we want the controlled system to achieve.



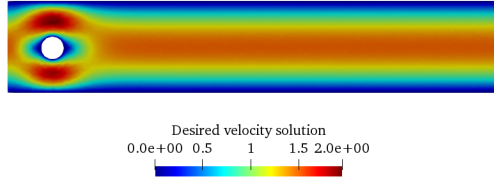


**Figure 3.** Experiment 1. Desired velocity profile  $U$ : steady Stokes flow ( $\nu = 1$ ).

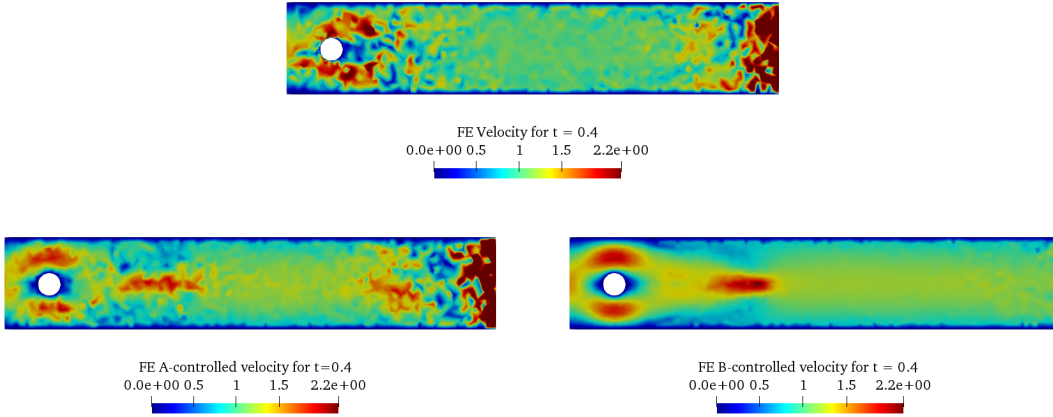


**Figure 4.** Experiment 1. Top plot: FE velocity profile for  $t = 0.4$ . No regularization is used. Bottom plot: A-controlled (left) and B-controlled (right) versions of the velocity profile for  $t = 0.4$  and  $\gamma = 1$ .

First, we stress that the problem we are dealing with needs stabilization if no control is applied<sup>1</sup>, since numerical oscillations arise even for small  $t$ . This is shown in Figure 4 (top), where we display the results at  $t = 0.4$  for a simulation without stabilization. The bottom panels in Figure 4 show two cases in which control is applied. From the bottom right panel, it is clear that the action of  $f_B$  stabilizes the flow in order to reach the desired configuration  $U$ . This does not hold for the A-controlled velocity (displayed in the bottom left panel in Figure 4), where spurious numerical oscillations are still displayed. This result agrees with our motivation for introducing  $f_B$  as a *stronger* control, especially tailored to treat higher Reynolds number flows with  $\nu \ll 1$ , while  $f_A$  was defined to deal with laminar settings where  $(\nu - K_0 \|U\|_{L^\infty((0,T);H^1(\Omega))}) > 0$ , namely  $\nu \sim 1$  (see Theorem 1).

In Figure 5, we represent the exponential convergence for the A-controlled and B-controlled systems, which we proved in section 3. We show the value of the *tracking error*,  $E_U(t) = \|u(t) - U(t)\|_{L^2(\Omega)}^2$ , for  $\gamma \in \{5, 1\}$  and  $t \in (0, 8)$  in the right plot of Figure 5. Similarly, the left panel shows the temporal evolution of  $E_U(t)$  when  $\gamma \in \{50, 25\}$  and  $t \in (0, 0.3)$ , where the considerably shorter time interval is justified by the fact that convergence is reached way before the final time  $T = 8$ . Indeed, for  $\gamma = 50$ ,  $E_U(t)$  is below machine precision already for  $t = 0.324$ . For the large values of  $\gamma \in \{50, 25\}$ , the two controls are comparable in terms of convergence. Differences between the A-controlled and B-controlled cases appear for smaller values of  $\gamma$ , i.e.,  $\gamma = 5$  and  $\gamma = 1$ . While for  $\gamma = 5$  the exponential convergence is preserved for both controls, we can observe that  $f_A$  does not converge to  $U$  for  $\gamma = 1$ , whereas  $f_B$  quickly converges to  $U$ . For these reasons, from now on, we will investigate the performances of the  $f_B$  control, which is more suited to problems

<sup>1</sup>The reader interested in the need for EFR in the uncontrolled context may refer to Appendix A.

where  $\gamma \ll 1$ , i.e., when the control action might not be sufficient to stabilize the simulation in the convective-dominated regime.

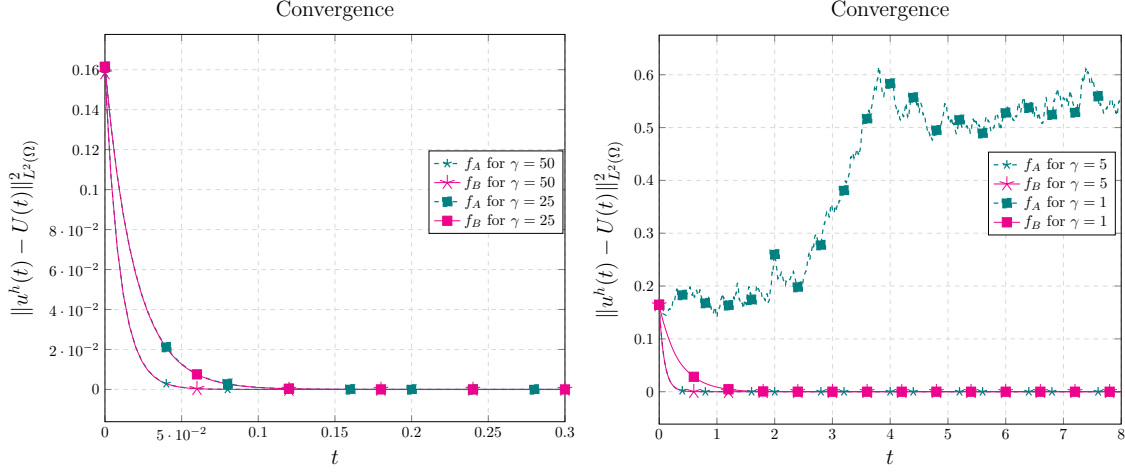


**Figure 5.** Experiment 1. Convergence results for  $f_A$  (teal dashed line) and  $f_B$  (magenta solid line) for  $\gamma \in \{50, 25, 5, 1\}$ . For  $\gamma = 50, 25, 5$ , the two approaches coincide.

**5.2. noEFR vs. EFR and aEFR Numerical Comparison (Experiment 2).** Following the discussion above, in what follows, we only consider the control  $f_B$ , which is more appropriate for high  $Re$  flows. A natural question arises: What happens to  $f_B$  as  $\gamma \rightarrow 0$ , namely for a weak control action, which is common in realistic applications.

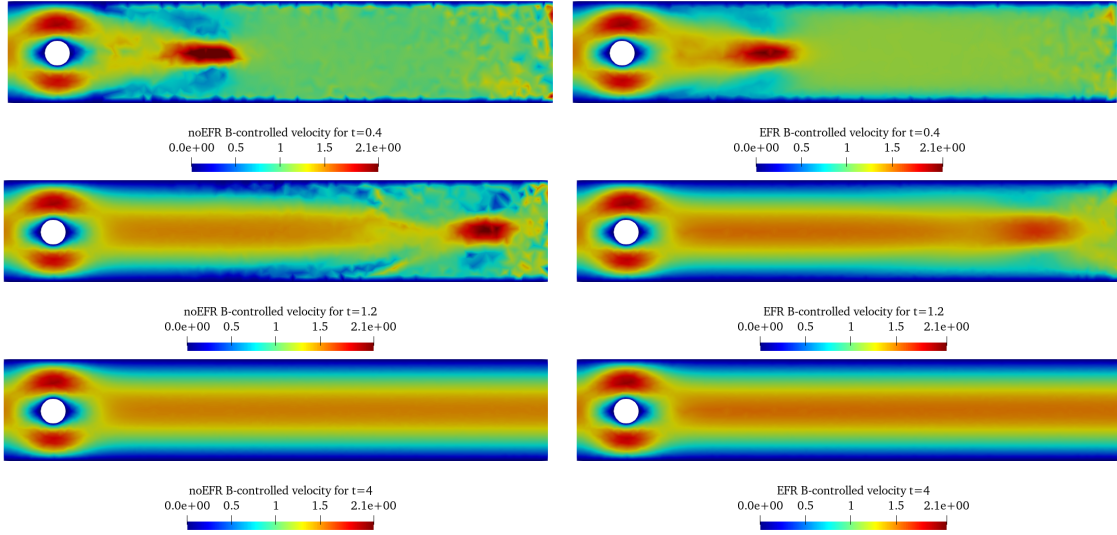


**Figure 6.** Experiment 2. Representative noEFR (left plots) and EFR (right plots) B-controlled velocity for  $t \in \{0.4, 1.2, 4\}$  (top to bottom) and  $\gamma = 10^{-4}$ . No qualitative difference can be observed between EFR and aEFR strategy; for clarity, the latter results are not shown.

We investigate this question in the same numerical setting proposed in section 5.1, with the only exception that  $T = 4$ . The reason for this choice is that the simulation is trivial for  $t > 4$ , when the behaviour of the controlled system is laminar and similar to the desired state  $U$ , which numerical

experiments in the previous section show to be reached already for  $t \sim 2$ . We show the results in Figures 6 and 7 for  $\gamma = 10^{-4}$ , which is a  $\gamma$  value considerably smaller than the values employed in the previous experiment. It is clear that such a small  $\gamma$  value slows down the convergence of the controlled solution  $u$  to the desired state  $U$  with respect to the cases in Experiment 1. From a qualitative point of view, such a conclusion is supported by a comparison of the top left plot of Figure 6 with the bottom right plot of Figure 4, representing B-controlled velocities at time instance  $t = 0.4$  for  $\gamma = 10^{-4}$  and  $\gamma = 1$ , respectively. The larger value  $\gamma = 1$  stabilizes numerical oscillations, which are instead more visible when  $\gamma = 10^{-4}$ , most of all at the end of the channel. These oscillations propagate in time within the channel (see the left center plot of Figure 6) until the convergence is reached at  $t = 4$  (see the left bottom plot of Figure 6). The spurious oscillations related to the small values of  $\nu$  and  $\gamma$  affect the exponential convergence of the problem, as depicted in Figure 7. Let us focus on the right plot: It is clear that the exponential convergence of the noEFR approach is affected for  $t \in (0, 2)$  by the spurious numerical oscillations, slowing down the achievement of the goal. Namely, there is a need for some other kind of stabilization, different from the control action, in order to get rid of the spurious numerical instabilities and reach the goal within a certain threshold in a shorter time. We employ the EFR strategy and analyze its effects on the control setting. For the EFR approach, we use the same parameters used in section A.1, i.e.,  $\delta = C_\delta \delta^*$  with  $C_\delta = \sqrt{11}$ ,  $\delta^* = 4.46 \cdot 10^{-3}$ , and  $\chi = 5 \cdot \Delta t$ . The reason behind this choice is explained in section A.1 for the uncontrolled setting. In the controlled framework, we employ the same parameters.

In the right plots of Figure 6, we see how the EFR strategy reduces the numerical oscillations, as expected. We stress that this is also helpful in the convergence behaviour. Indeed, lower values of the objective  $E_U$  are reached in a shorter time, as can be observed from the dashed orange line of Figure 7.

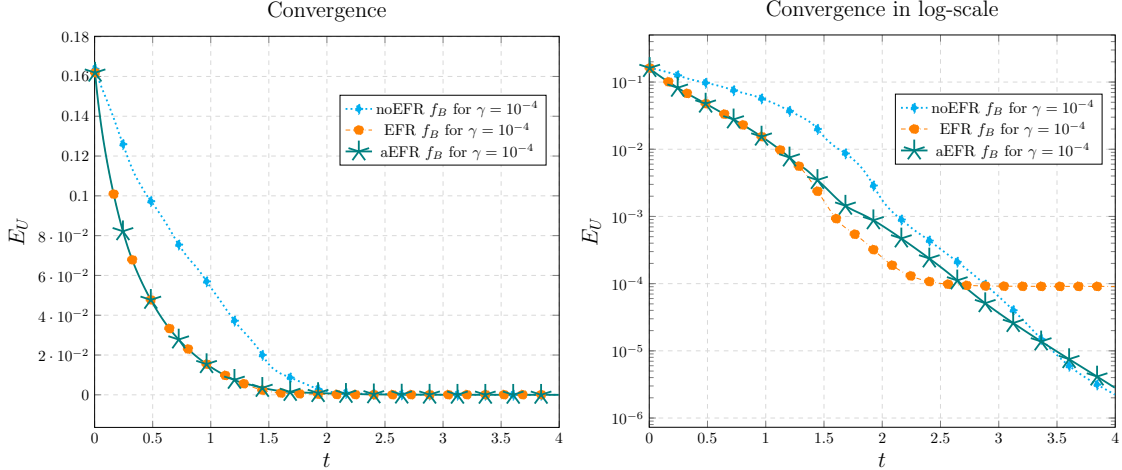


**Figure 7.** Experiment 2. Convergence results for noEFR (dotted cyan line), EFR (orange dashed line), and aEFR (solid teal line)  $f_B$  velocity with  $\gamma = 10^{-4}$ . The left plot is displayed on a log-scale on the right.

We remark that, although we do not recover the exponential decay in the EFR case, we do obtain significantly better results than the noEFR results:

- The EFR approach alleviates the spurious numerical oscillations. Thus, we can expect a better convergence rate with respect to noEFR in the first part of the time interval. We note, however, that the exponential convergence of Theorem 2 is not guaranteed, as shown in Theorem 5.
- The EFR strategy reaches the steady state profile with an accuracy of  $O(10^{-4})$  more than 0.5 time units before the noEFR approach, i.e., at  $t = 2.5$  instead of  $t = 2.9$ .

Despite the increased accuracy in the first part of the simulation, the EFR control reaches a plateau for  $t > 2.5$ , and  $E_U \sim 10^{-4}$  after that time instance. Indeed, once the convergence is reached, i.e., when the profile is laminar, the EFR is unnecessarily over-diffusing. This leads to a more inaccurate reconstruction with respect to the noEFR approach. However, for small  $\gamma$  and  $\nu$  values, noEFR does not show an exponential convergence at the beginning of the simulation, while EFR does. The EFR stagnation issue is overcome through the employment of the new aEFR approach with  $\tau \sim 0.006$ . The choice of the  $\tau$  value is guided by the EFR simulation: We stopped the EFR simulation before it reached the plateau.

By definition, aEFR performs as EFR until  $E_U \geq \tau$ , i.e., for  $t < 1.46$ . After that time instance, the standard controlled Navier-Stokes simulation is performed. For the sake of brevity, we do not show the representative solutions for the aEFR strategy, since there are no visible qualitative differences from the right plots of Figure 6. The advantages of using aEFR are clear in the right plot of Figure 7 (solid teal line), where the exponential convergence is recovered as in the noEFR system avoiding the plateau effect of the EFR strategy. The aEFR approach guarantees  $E_U \sim 10^{-4}$  for  $t = 2.65$  (before the noEFR approach, which reaches a similar threshold around  $t = 2.9$ ). For  $t > 2.65$ , the aEFR strategy achieves exponential convergence, and by  $T = 4$  noEFR and aEFR are comparable. Based on these results, in what follows, we will exclusively employ the aEFR strategy.

**5.3. aEFR-noEFR vs. aEFR-aEFR Numerical Comparison (Experiment 3).** In this section, we compare two approaches: (i) aEFR-noEFR, i.e., the standard G-ROM with no regularization at the ROM level; and (ii) aEFR-aEFR, which employs the aEFR regularization at the ROM level. In the FOM setting, we perform the aEFR strategy, as presented in section 5.2. All the parameters of the FOM discretization are defined in section 5.1. Furthermore, for the aEFR-aEFR strategy, the parameters used at the FOM level are also used at the ROM level, in agreement with the FOM-ROM consistency strategy proposed in [71]. For the ROM, we apply a POD approach over 1000 equispaced snapshots in the time interval  $(0, 4)$ . The ROM solution is represented by  $r_u = 20$  basis functions for the velocity and  $r_p = r_s = 1$  basis functions for the pressure and the supremizer. These values follow a retained information criterion. In Table 3, we observe that  $r_u = 20$  preserves 98% of the velocity information of the system, which is the value we choose as a retained information threshold. For the pressure, the value  $r_p = 1$  is already enough to represent 99% of the pressure retained information. For the sake of completeness, in Table 3, we report the retained information values for  $r_u$  in the set  $\{1, 10, 15, 20\}$ .

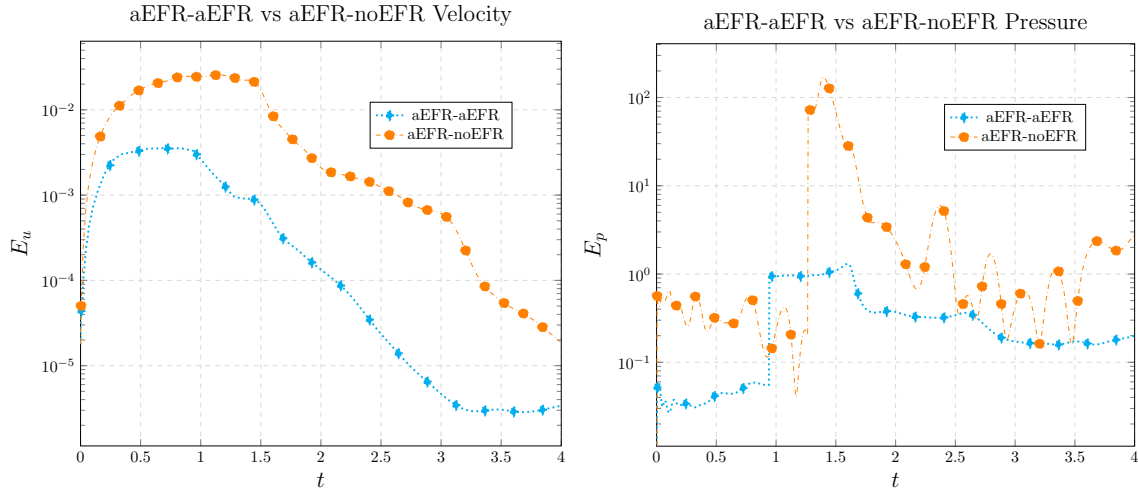


**Figure 8.** Experiment 3. Relative errors between aEFR-noEFR (dotted cyan line) and aEFR-aEFR (dashed orange line)  $f_B$  controlled velocity (left) and pressure (right) with  $\gamma = 10^{-4}$ .

We test the accuracy of the method by means of the relative errors for velocity and pressure at each time instance, defined, respectively, as

$$E_u(t^n) = \frac{\|u^n - u_r^n\|_{L^2(\Omega)}^2}{\|u^n\|_{L^2(\Omega)}^2} \quad \text{and} \quad E_p(t^n) = \frac{\|p^n - p_r^n\|_{L^2(\Omega)}^2}{\|p^n\|_{L^2(\Omega)}^2},$$

where  $u^n$  is the FOM aEFR velocity at time  $t_n$ , and  $u_r^n$  is the reduced velocity (either aEFR-noEFR or aEFR-aEFR). Similar notations are employed for the pressure. In Figure 8, we plot the log-relative errors  $E_u$  (left plot) and  $E_p$  (right plot) for the aEFR-noEFR and aEFR-aEFR approaches. The employment of aEFR strategy at the ROM level is beneficial in terms of accuracy for both variables. Focusing on the velocity, the gain in accuracy reaches two orders of magnitude for  $t = 3$ , where  $E_u$  reaches  $10^{-3}$  and  $10^{-5}$  for aEFR-noEFR and aEFR-aEFR, respectively. The same happens with the pressure at  $t = 1.5$ , where  $E_p$  reaches  $10^2$  and 1 for aEFR-noEFR and aEFR-aEFR, respectively. For the velocity, at all the time instances, the aEFR-aEFR is more accurate. We can state the same for the pressure, except for  $t \in (0.9, 1.3)$ .

**Table 3.** Experiment 3. Information retained by the POD basis functions for velocity and pressure.

$r_u = r_p$	Velocity information	Pressure information
1	53%	99%
10	95%	99%
15	97%	99%
20	98%	99%

In order to illustrate the better performance in terms of accuracy of aEFR-aEFR with respect to aEFR FOM solution, we show representative solutions for velocity and pressure in Figure 9 and Figure 10, respectively. We compare aEFR-aEFR and aEFR with the aEFR-noEFR technique. For the velocity, we analyze the results at  $t = 1$ , i.e., at a time instance where we can observe an increasing trend of  $E_u$  for the aEFR-noEFR velocity. From the plot, we observe that the aEFR-noEFR velocity presents some spurious oscillations in the second half of the channel, i.e., for  $y > 1$ . I thought that  $0 < y < 0.41$  as defined in  $\Omega$ . These oscillations are alleviated by the aEFR-aEFR approach, leading to a solution that is more similar to the aEFR FOM solution. For the pressure, we see that the aEFR-noEFR strategy is off with respect to the aEFR solution. The aEFR-aEFR pressure is more similar and, moreover, alleviates the spurious oscillations that are still present at the end of the channel in the FOM simulation. We conclude that the aEFR-aEFR strategy is more accurate than the aEFR-noEFR approach. We also emphasize that no extra computational effort is needed in the aEFR-aEFR strategy since the filtering and the relaxation steps are not computationally expensive and are used only for the first part of the simulation.

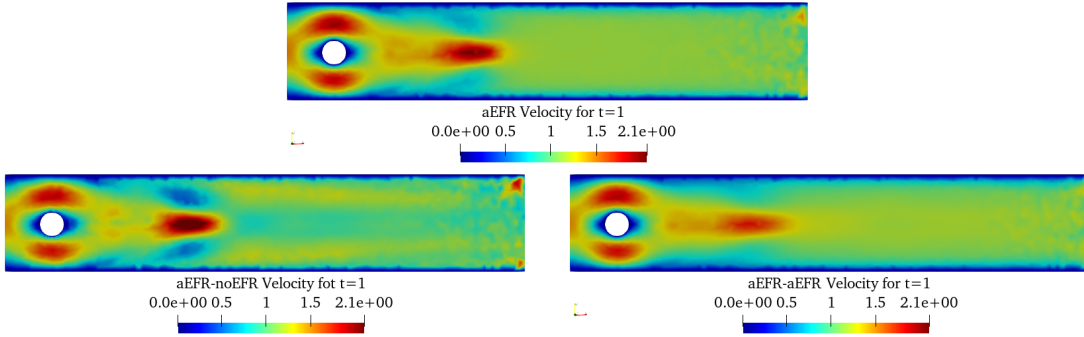


**Figure 9.** Experiment 3. Top plot: aEFR velocity profile for  $t = 1$ . Bottom plots: aEFR-noEFR (left) and aEFR-aEFR (right) velocity profiles for  $t = 1$  and  $\gamma = 10^{-4}$ .

The benefits of using the aEFR-aEFR strategy are evident from the convergence plots in Figure 11, where the tracking error  $E_U^r = \|\mathbf{Q}_{U^{r,u,s}}^T u_r^n - U^n\|_{L^2(\Omega)}^2$  is plotted against time. The aEFR-aEFR strategy stabilizes the system and reaches the desired state  $U$  in a shorter time, recovering the exponential convergence proved at the FOM level. In particular, we note that the aEFR-aEFR velocity reaches  $E_U^r \sim 10^{-4}$  at  $t = 2.75$ , almost a time unit before the aEFR-noEFR strategy. Thus, the aEFR-aEFR approach is not only more accurate but also reaches the goal faster. These benefits are not related to an increased algorithmic complexity during the ROM evaluation (for both techniques the speedup<sup>2</sup>, i.e., the number of ROM simulations one can perform in the time of a FOM simulation, is around 2) and, thus, the aEFR-aEFR strategy is competitive with respect to the aEFR-noEFR technique in terms of computational costs.

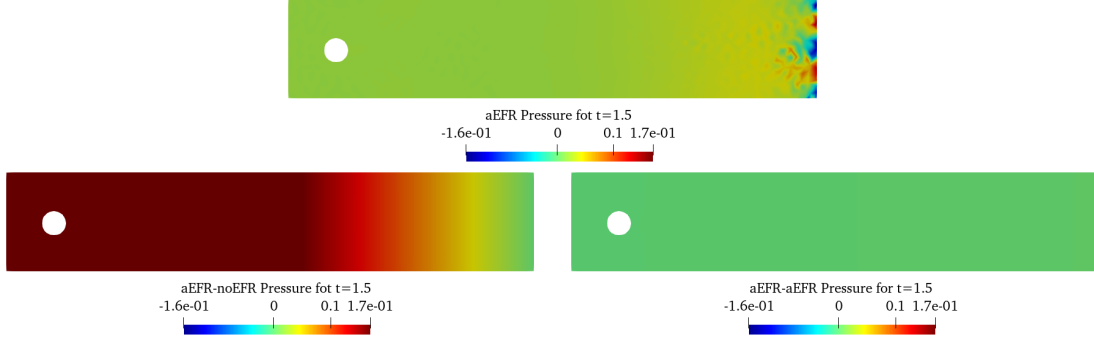


**Figure 10.** Experiment 3. Top plot: aEFR pressure profile for  $t = 1$ . Bottom plot: aEFR-noEFR (left) and aEFR-aEFR (right) pressure profiles for  $t = 1$  and  $\gamma = 10^{-4}$ . We stress that the values of the aEFR-aEFR pressure profile are not exactly zero, but range between  $10^{-3}$  and  $10^{-2}$ .

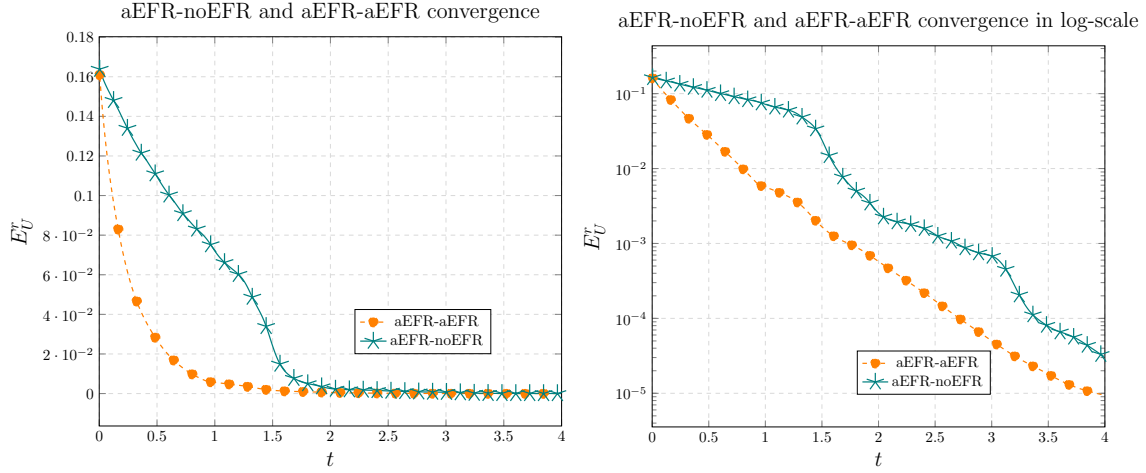


**Figure 11.** Experiment 3. Convergence results for aEFR-noEFR (solid teal line) and aEFR-aEFR (dashed orange line). The left plot is replotted on a log-scale on the right.

<sup>2</sup>The ROM simulation depends on the FOM dimension affecting the speedup value. The online computational costs decrease if hyper-reduction techniques, such as the empirical interpolation method (EIM), are employed. The interested reader may refer to [12] or [38, Chapter 5]. However, the application of this kind of algorithm was beyond the scope of this work.

## 6. CONCLUSIONS

In this paper, we proposed a novel feedback control strategy for the incompressible Navier-Stokes equations (NSE) at high Reynolds numbers. For the continuous case, in Theorem 2 we proved that the new feedback control strategy yields accurate results for high Reynolds numbers that were not covered by Theorem 1 for the feedback law proposed in [33]. For the discrete (finite element) case, we proved in Theorem 4 that the new feedback control strategy is accurate for high Reynolds numbers for which Theorem 3 in [33] does not apply. In Section 5, we compared the new feedback control strategy with the standard approach in the marginally-resolved numerical simulations of a two-dimensional flow past a circular cylinder at Reynolds numbers  $Re = 1000$ . The numerical results showed that the new feedback control yields more accurate results than the standard control.

Our second contribution is the development of an adaptive evolve-filter-relax (aEFR) regularization for both the FOM and the ROM feedback control settings. Our numerical investigation shows that the novel aEFR stabilizes marginally-resolved simulations at high Reynolds numbers and increases the accuracy of the new feedback control for realistic control parameters (i.e., when the magnitude of the feedback control is relatively low). Specifically, the new aEFR strategy yields more accurate results than the classical EFR approach, especially toward the end of the numerical simulation. Furthermore, both aEFR and EFR are significantly more accurate than the noEFR approach (i.e., when no regularization is used), especially at the beginning of the numerical simulation.

The first steps in the theoretical and numerical investigation of the novel feedback control and aEFR algorithm are encouraging. There are several research directions for the further study of these strategies. For example, other regularized ROMs (such as the Leray ROM [74]) could be analyzed and investigated numerically within the new feedback control framework. The new feedback control and aEFR algorithm could also be studied in the numerical simulation and control of higher Reynolds number turbulent flows. Finally, rigorous mathematical support should be provided for the EFR and aEFR strategies within the new feedback control framework.

## ACKNOWLEDGMENTS

We acknowledge the European Union’s Horizon 2020 research and innovation program under the Marie Skłodowska-Curie Actions, grant agreement 872442 (ARIA). MS and CC thank the MIUR project “Dipartimenti di Eccellenza 2018-2022” (CUP E11G18000350001). MS and FB acknowledge the INdAM-GNCS project “Metodi numerici per lo studio di strutture geometriche parametriche complesse” (CUP E53C22001930001). FB also thanks the project “Reduced order modelling for numerical simulation of partial differential equations” funded by Università Cattolica del Sacro Cuore. TI acknowledges support through National Science Foundation grants DMS-2012253 and CDS&E-MSS-1953113.

The computations in this work have been performed with RBniCS [1] library, which is an implementation in FEniCS [49] of several reduced order modeling techniques; we acknowledge developers and contributors to both libraries. Computational resources were partially provided by HPC@POLITO, a project of Academic Computing within the Department of Control and Computer Engineering at the Politecnico di Torino (<http://hpc.polito.it>).

## REFERENCES

- [1] RBniCS – reduced order modelling in FEniCS, <https://www.rbnicsproject.org/>.
- [2] A. Alla, M. Falcone, and L. Saluzzi. An efficient DP algorithm on a tree-structure for finite horizon optimal control problems. *SIAM Journal of Scientific Computing*, 41(4):2384–2406, 2019.
- [3] A. Alla, M. Falcone, and L. Saluzzi. A tree structure algorithm for optimal control problems with state constraints. *Rendiconti di Matematica e delle Sue Applicazioni*, 41:193–221, 2020.
- [4] A. Alla, M. Falcone, and S. Volkwein. Error analysis for POD approximations of infinite horizon problems via the dynamic programming approach. *SIAM Journal on Control and Optimization*, 55(5):3091–3115, 2017.
- [5] A. Alla and M. Hinze. HJB-POD feedback control for Navier-Stokes equations. In G. Russo, V. Capasso, G. Nicosia, and V. Romano, editors, *Progress in Industrial Mathematics at ECMI 2014*, pages 861–868, Cham, 2016. Springer International Publishing.

- [6] A. Alla and L. Saluzzi. A HJB-POD approach for the control of nonlinear PDEs on a tree structure. *Appl Numer Math.*, 155:192–207, 2020.
- [7] F. Ballarin, A. Manzoni, A. Quarteroni, and G. Rozza. Supremizer stabilization of POD–Galerkin approximation of parametrized steady incompressible Navier–Stokes equations. *Int. J. Numer. Meth. Engng.*, 102:1136–1161, 2015.
- [8] F. Ballarin, G. Rozza, and M. Strazzullo. Chapter 9 - space-time POD-Galerkin approach for parametric flow control. In E. Trélat and E. Zuazua, editors, *Numerical Control: Part A*, volume 23 of *Handbook of Numerical Analysis*, pages 307–338. Elsevier, 2022.
- [9] E. Bänsch, P. Benner, J. Saak, and H. K. Weichelt. Riccati-based boundary feedback stabilization of incompressible Navier–Stokes flows. *SIAM Journal on Scientific Computing*, 37(2):A832–A858, 2015.
- [10] V. Barbu. Feedback stabilization of Navier–Stokes equations. *ESAIM: Control, Optimisation and Calculus of Variations*, 9:197–205, 2003.
- [11] V. Barbu and R. Triggiani. Internal stabilization of Navier–Stokes equations with finite-dimensional controllers. *Indiana University Mathematics Journal*, 53(5):1443–1494, 2004.
- [12] M. Barrault, Y. Maday, N. C. Nguyen, and A. T. Patera. An ‘empirical interpolation’ method: Application to efficient reduced-basis discretization of partial differential equations. *C. R. Acad. Sci. Paris, Ser. I*, 339:667–672, 2004.
- [13] P. Benner, S. Dolgov, A. Onwunta, and M. Stoll. Low-rank solution of an optimal control problem constrained by random Navier–Stokes equations. *International Journal for Numerical Methods in Fluids*, 92(11):1653–1678, 2020.
- [14] P. Benner and C. Trautwein. Optimal control problems constrained by the stochastic Navier–Stokes equations with multiplicative Lévy noise. *Mathematische Nachrichten*, 292(7):1444–1461, 2019.
- [15] L. Bertagna, A. Quaini, and A. Veneziani. Deconvolution-based nonlinear filtering for incompressible flows at moderately large Reynolds numbers. *Int. J. Num. Meth. Fluids*, 81(8):463–488, 2016.
- [16] J. Burkardt, M. Gunzburger, and H. Lee. POD and CVT-based reduced-order modeling of Navier–Stokes flows. *Comput. Methods Appl. Mech. Engng.*, 196(1-3):337–355, 2006.
- [17] S. Collis, R. Joslin, A. Seifert, and V. Theofilis. Issues in active flow control: theory, control, simulation, and experiment. *Progress in Aerospace Sciences*, 40(4-5):237–289, 2004. cited By 278.
- [18] S. S. Collis and M. Heinkenschloss. Analysis of the streamline upwind/Petrov Galerkin method applied to the solution of optimal control problems. *CAAM TR02-01*, 108, 2002.
- [19] K. Deckelnick and M. Hinze. Semidiscretization and error estimates for distributed control of the instationary Navier–Stokes equations. *Numerische Mathematik*, 97(2):297 – 320, 2004.
- [20] L. Dedè. Reduced basis method and error estimation for parametrized optimal control problems with control constraints. *Journal of Scientific Computing*, 50(2):287–305, Feb 2012.
- [21] S. Dolgov, D. Kalise, and L. Saluzzi. Data-driven tensor train gradient cross approximation for Hamilton–Jacobi–Bellman equations. *arXiv preprint arXiv:2205.05109*, 2022.
- [22] V. J. Ervin, W. J. Layton, and M. Neda. Numerical analysis of filter-based stabilization for evolution equations. *SIAM J. Numer. Anal.*, 50(5):2307–2335, 2012.
- [23] M. Falcone, G. Kirsten, and L. Saluzzi. Approximation of optimal control problems for the Navier–Stokes equation via multilinear HJB-POD. *Applied Mathematics and Computation*, 442:127722, 2023.
- [24] P. F. Fischer and J. Mullen. Filter-based stabilization of spectral element methods. *C. R. Acad. Sci. Paris Sér. I Math.*, 332(3):265–270, 2001.
- [25] U. Frisch. *Turbulence, The Legacy of A.N. Kolmogorov*. Cambridge University Press, Cambridge, 1995.
- [26] A. Fürsikov, M. Gunzburger, L. S. Hou, and S. Manservigi. Optimal control problems for the Navier–Stokes equations. In H.-J. Bungartz, R. H. W. Hoppe, and C. Zenger, editors, *Lectures on Applied Mathematics*, pages 143–155. Berlin, Heidelberg, 2000. Springer Berlin Heidelberg.
- [27] M. Girfoglio, A. Quaini, and G. Rozza. A POD–Galerkin reduced order model for a LES filtering approach. *J. Comput. Phys.*, 436:110260, 2021.
- [28] M. Girfoglio, A. Quaini, and G. Rozza. Pressure stabilization strategies for a LES filtering reduced order model. *Fluids*, 6(9), 2021.
- [29] M. Girfoglio, A. Quaini, and G. Rozza. A POD-galerkin reduced order model for the Navier–Stokes equations in stream function-vorticity formulation. *Computers & Fluids*, 244:105536, 2022.
- [30] M. Girfoglio, A. Quaini, and G. Rozza. A hybrid projection/data-driven reduced order model for the Navier–Stokes equations with nonlinear filtering stabilization. *Journal of Computational Physics*, 486:112127, 2023.
- [31] S. Grimberg, C. Farhat, and N. Youkilis. On the stability of projection-based model order reduction for convection-dominated laminar and turbulent flows. *J. Comput. Phys.*, 419:109681, 2020.
- [32] M. Gunzburger, T. Iliescu, and M. Schneier. A Leray regularized ensemble-proper orthogonal decomposition method for parameterized convection-dominated flows. *IMA J. Numer. Anal.*, 40(2):886–913, 2020.
- [33] M. Gunzburger and S. Manservigi. Analysis and approximation for linear feedback control for tracking the velocity in Navier–Stokes flows. *Computer Methods in Applied Mechanics and Engineering*, 189(3):803–823, 2000.
- [34] M. D. Gunzburger. *Perspectives in flow control and optimization*. SIAM, 2002.



- [35] M. D. Gunzburger, L. Hou, and T. P. Svobodny. Analysis and finite element approximation of optimal control problems for the stationary Navier-Stokes equations with distributed and Neumann controls. *Mathematics of Computation*, 57(195):123–151, 1991.
- [36] M. D. Gunzburger and S. Manservigi. Analysis and approximation of the velocity tracking problem for Navier-Stokes flows with distributed control. *SIAM Journal on Numerical Analysis*, 37(5):1481–1512, 2000.
- [37] M. Heinkenschloss, D. C. Sorensen, and K. Sun. Balanced truncation model reduction for a class of descriptor systems with application to the Oseen equations. *SIAM Journal on Scientific Computing*, 30(2):1038–1063, 2008.
- [38] J. S. Hesthaven, G. Rozza, and B. Stamm. *Certified Reduced Basis Methods for Parametrized Partial Differential Equations*. Springer, 2015.
- [39] M. Hinze. Instantaneous closed loop control of the Navier–Stokes system. *SIAM Journal on Control and Optimization*, 44(2):564–583, 2005.
- [40] M. Hinze and K. Kunisch. Three control methods for time-dependent fluid flow. *Flow, Turbulence and Combustion*, 65(3-4):273–298, 2000.
- [41] K. Kaneko, P.-H. Tsai, and P. Fischer. Towards model order reduction for fluid-thermal analysis. *Nucl. Eng. Des.*, 370:110866, 2020.
- [42] M. Kärcher and M. A. Grepl. A posteriori error estimation for reduced order solutions of parametrized parabolic optimal control problems. *ESAIM: Mathematical Modelling and Numerical Analysis*, 48(6):1615–1638, 2014.
- [43] M. Kärcher, Z. Tokoutsi, M. A. Grepl, and K. Veroy. Certified reduced basis methods for parametrized elliptic optimal control problems with distributed controls. *Journal of Scientific Computing*, 75(1):276–307, 2018.
- [44] K. Kunisch and S. Volkwein. Proper orthogonal decomposition for optimality systems. *ESAIM: Math. Model. Numer. Anal.*, 42(1):1–23, 2008.
- [45] W. Layton, C. C. Manica, M. Neda, and L. G. Rebholz. Numerical analysis and computational testing of a high accuracy Leray-deconvolution model of turbulence. *Nucl. Meth. P.D.E.s*, 24(2):555–582, 2008.
- [46] W. J. Layton. *Introduction to the numerical analysis of incompressible viscous flows*, volume 6. Society for Industrial and Applied Mathematics (SIAM), 2008.
- [47] H.-C. Lee. Efficient computations for linear feedback control problems for target velocity matching of Navier-Stokes flows via POD and LSTM-ROM. *Electronic Research Archive*, 29(3):2533–2552, 2021.
- [48] D. Leykekhman and M. Heinkenschloss. Local error analysis of discontinuous Galerkin methods for advection-dominated elliptic linear-quadratic optimal control problems. *SIAM Journal on Numerical Analysis*, 50(4):2012–2038, 2012.
- [49] A. Logg, K. Mardal, and G. Wells. *Automated Solution of Differential Equations by the Finite Element Method*. Springer-Verlag, Berlin, 2012.
- [50] E. Mallea-Zepeda, E. Ortega-Torres, and É. J. Villamizar-Roa. An optimal control problem for the Navier-Stokes- $\alpha$  system. *J. Dyn. Control Syst.*, pages 1–28, 2021.
- [51] J. S. Mullen and P. F. Fischer. Filtering techniques for complex geometry fluid flows. *Commun. Numer. Meth. Engrg.*, 15(1):9–18, 1999.
- [52] F. Negri, A. Manzoni, and G. Rozza. Reduced basis approximation of parametrized optimal flow control problems for the Stokes equations. *Computers & Mathematics with Applications*, 69(4):319–336, 2015.
- [53] F. Negri, G. Rozza, A. Manzoni, and A. Quarteroni. Reduced basis method for parametrized elliptic optimal control problems. *SIAM Journal on Scientific Computing*, 35(5):A2316–A2340, 2013.
- [54] B. R. Noack, M. Morzynski, and G. Tadmor. *Reduced-Order Modelling for Flow Control*, volume 528. Springer Verlag, 2011.
- [55] E. J. Parish, M. Yano, I. Tezaur, and T. Iliescu. Residual-based stabilized reduced-order models of the transient convection-diffusion-reaction equation obtained through discrete and continuous projection. *arXiv preprint, <http://arxiv.org/abs/2302.09355>*, 2023.
- [56] F. Pichi, M. Strazzullo, F. Ballarin, and G. Rozza. Driving bifurcating parametrized nonlinear PDEs by optimal control strategies: Application to Navier-Stokes equations with model order reduction. *ESAIM: Mathematical Modelling and Numerical Analysis*, 56(4):1361 – 1400, 2022.
- [57] S. Pope. *Turbulent flows*. Cambridge University Press, Cambridge, 2000.
- [58] A. Quarteroni and S. Quarteroni. *Numerical models for differential problems*, volume 2. Springer, 2009.
- [59] A. Quarteroni, G. Rozza, and A. Quaini. Reduced basis methods for optimal control of advection-diffusion problems. In *Advances in Numerical Mathematics*, number CMCS-CONF-2006-003, pages 193–216. RAS and University of Houston, 2007.
- [60] A. Quarteroni and A. Valli. *Numerical approximation of partial differential equations*, volume 23. Springer Science & Business Media, 2008.
- [61] J.-P. Raymond. Local boundary feedback stabilization of the Navier-Stokes equations. *Control Systems: Theory, Numerics and Applications, Rome*, 30, 2005.
- [62] J.-P. Raymond. Feedback boundary stabilization of the two-dimensional Navier–Stokes equations. *SIAM Journal on Control and Optimization*, 45(3):790–828, 2006.
- [63] J.-P. Raymond. Feedback boundary stabilization of the three-dimensional incompressible Navier–Stokes equations. *Journal de Mathématiques Pures et Appliquées*, 87(6):627–669, 2007.
- [64] G. Rozza and K. Veroy. On the stability of the reduced basis method for Stokes equations in parametrized domains. *Comput. Methods Appl. Mech. Engrg.*, 196(7):1244–1260, 2007.

- [65] F. Sabetghadam and A. Jafarpour.  $\alpha$  regularization of the POD-Galerkin dynamical systems of the Kuramoto–Sivashinsky equation. *Appl. Math. Comput.*, 218(10):6012–6026, 2012.
- [66] M. Schäfer and S. Turek. The benchmark problem ‘flow around a cylinder’ flow simulation with high performance computers II. in *E.H. Hirschel (Ed.), Notes on Numerical Fluid Mechanics*, 52, Braunschweig, Vieweg:547–566, 1996.
- [67] G. Stabile, F. Ballarin, G. Zuccharino, and G. Rozza. A reduced order variational multiscale approach for turbulent flows. *Adv. Comput. Math.*, pages 1–20, 2019.
- [68] M. Strazzullo, F. Ballarin, and G. Rozza. POD-Galerkin model order reduction for parametrized time dependent linear quadratic optimal control problems in saddle point formulation. *Journal of Scientific Computing*, 83(55), 2020.
- [69] M. Strazzullo, F. Ballarin, and G. Rozza. A Certified Reduced Basis method for linear parametrized parabolic optimal control problems in space-time formulation. Submitted, 2021, <https://arxiv.org/abs/2103.00460>.
- [70] M. Strazzullo, F. Ballarin, and G. Rozza. POD-Galerkin model order reduction for parametrized nonlinear time dependent optimal flow control: an application to Shallow Water Equations. *Journal of Numerical Mathematics*, 30(1):63–84, 2022.
- [71] M. Strazzullo, M. Girfoglio, F. Ballarin, T. Iliescu, and G. Rozza. Consistency of the full and reduced order models for evolve-filter-relax regularization of convection-dominated, marginally-resolved flows. *International Journal for Numerical Methods in Engineering*, 123(14):3148–3178, 2022.
- [72] M. Strazzullo, Z. Zainib, F. Ballarin, and G. Rozza. Reduced order methods for parametrized nonlinear and time dependent optimal flow control problems: towards applications in biomedical and environmental sciences. *Numerical Mathematics and Advanced Applications ENUMATH 2019*, 2021.
- [73] R. Temam. *Navier-Stokes equations: Theory and numerical analysis*, volume 2. American Mathematical Society, 2001.
- [74] D. Wells, Z. Wang, X. Xie, and T. Iliescu. An evolve-then-filter regularized reduced order model for convection-dominated flows. *Int. J. Num. Meth. Fluids*, 84:598–615, 2017.
- [75] X. Xie, D. Wells, Z. Wang, and T. Iliescu. Numerical analysis of the Leray reduced order model. *J. Comput. Appl. Math.*, 328:12–29, 2018.
- [76] F. Zoccolan, M. Strazzullo, and G. Rozza. Stabilized weighted reduced order methods for parametrized advection-dominated optimal control problems governed by partial differential equations with random inputs. *arXiv preprint arXiv:2301.01975*, 2023.
- [77] F. Zoccolan, M. Strazzullo, and G. Rozza. A streamline upwind Petrov-Galerkin reduced order method for advection-dominated partial differential equations under optimal control. *arXiv preprint arXiv:2301.01973*, 2023.

## APPENDIX A. EFR AND EFR-EFR FOR NSE: A PARAMETRIC STUDY

This section is a numerical investigation of the increased stability and accuracy of the EFR strategy for FOM and ROM marginally-resolved simulations. We perform two numerical experiments.

- *Experiment A1.* A numerical comparison between noEFR and EFR at the FOM level. In particular, this experiment analyzes the performance of the EFR algorithm for different  $\delta$  values, providing guidelines for the numerical setting of section 5.
- *Experiment A2.* A numerical comparison between noEFR and EFR at the ROM level for POD basis functions obtained by using the EFR regularization.

**A.1. noEFR vs. EFR Numerical Comparison (Experiment A1).** In this section, we perform a numerical investigation of the role played by the EFR strategy in marginally-resolved FOM simulations. To this end, we compare the following two approaches: (i) noEFR, which is a standard numerical discretization of the NSE without the EFR regularization; and (ii) EFR, which is a numerical discretization of the NSE with the EFR regularization. We now focus on the uncontrolled framework, which is extended to the feedback control setting in section 3. In this section, we solve problem (1). The domain and the boundary conditions are those used in section 5.2. The initial condition is  $u_0 = (0, 0)$ , the time interval is  $(0, 4)$ , and the time step is  $\Delta t = 4 \cdot 10^{-4}$ . We use a test case that highlights the drawbacks of the noEFR procedure in marginally-resolved regimes. We remark that, differently from [71], where the range of the Reynolds number is  $0 \leq Re \leq 100$ , we work with a Reynolds number that is one order of magnitude higher:  $Re = 1000$ . The first questions we address are: (i) How do the mesh parameters affect the stability of the noEFR solutions? and (ii) Are the simulations accurate? The numerical investigation employs four meshes: M1, M2, M3, and M4. M1 is the mesh depicted in Figure 2. We recall that the mesh parameters are  $h_{min} = 4.46 \cdot 10^{-3}$  and  $h_{max} = 4.02 \cdot 10^{-2}$ . To solve the system, we employ the Taylor-Hood  $\mathbb{P}^2 - \mathbb{P}^1$  finite element

discretization for velocity and pressure, respectively, with  $N_h \doteq N_h^u + N_h^p = 14053$  degrees of freedom. M2 is a finer mesh with  $h_{min} = 4.45 \cdot 10^{-3}$  and  $h_{max} = 1.67 \cdot 10^{-2}$ , and  $N_h = 68117$ . We also analyze the performance of M3, a finer mesh with respect to M2 and M1, with  $h_{min} = 4.45 \cdot 10^{-3}$  and  $h_{max} = 1.49 \cdot 10^{-2}$ , and  $N_h = 93076$ . The finest mesh is M4, with  $h_{min} = 4.44 \cdot 10^{-3}$  and  $h_{max} = 1.13 \cdot 10^{-2}$ , and  $N_h = 113436$ . Table 4 summarizes the parameters of the four meshes.

**Table 4.** Experiment A1. Comparison of the M1, M2, M3, and M4 with respect to  $h_{min}$ ,  $h_{max}$ , and number of degrees of freedom.

mesh	$h_{min}$	$h_{max}$	$N_h$
M1	$4.46 \cdot 10^{-3}$	$4.02 \cdot 10^{-2}$	14053
M2	$4.45 \cdot 10^{-3}$	$1.67 \cdot 10^{-2}$	68117
M3	$4.45 \cdot 10^{-3}$	$1.49 \cdot 10^{-2}$	93076
M4	$4.44 \cdot 10^{-3}$	$1.13 \cdot 10^{-2}$	113436

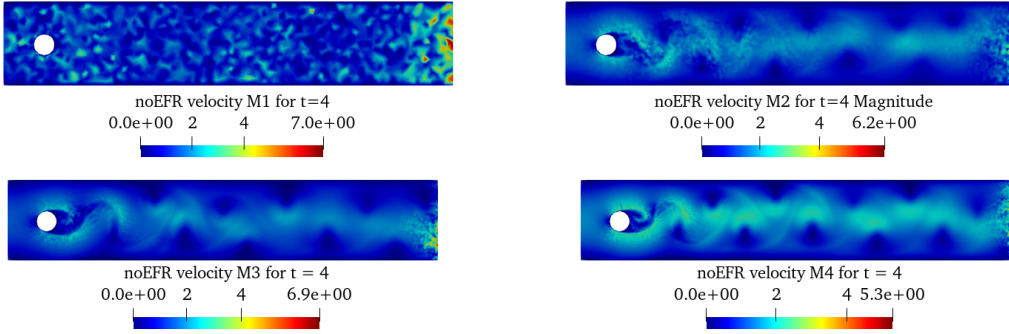


**Figure 12.** Experiment A1. noEFR vs EFR. noEFR velocity profile for  $t = 4$  and M1 (top left plot), M2 (top right plot), M3 (bottom left plot), and M4 (bottom right plot).

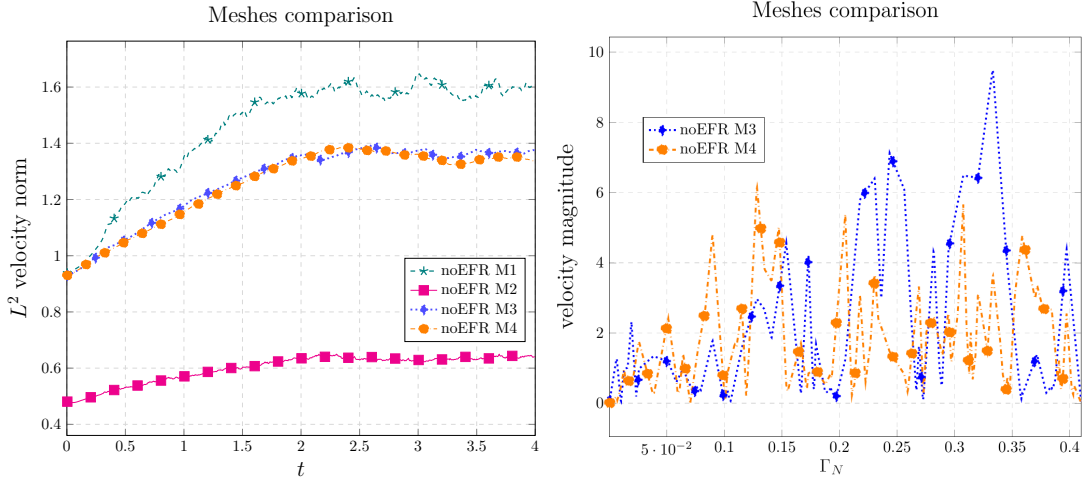


**Figure 13.** Experiment A1. noEFR vs EFR.  $L^2$  velocity norm and velocity magnitude over  $\Gamma_N$  for M1 (dashed green line), M2 (solid magenta line), and M3 (dashed-dotted orange line), left and right plot, respectively.

With M1, as stated in [71], we work in a marginally-resolved regime. For high Reynolds number values, the simulation does not capture the features of the flow, presenting numerical oscillations, as

illustrated in the top left plot of Figure 12. The numerical oscillations are alleviated by decreasing the value of  $h_{max}$ . For M2, we can observe some oscillations just behind the cylinder and at the end of the channel. These oscillations remain even by decreasing the value of  $h_{max}$ , as done for M3 and M4. However, these meshes are capable of smoothly representing the vortex shedding. Moreover, the  $L^2$ -norm plot in Figure 13 shows that the numerical results on M3 and M4 are comparable, and their norms converge, whereas the numerical results on M1 and M2 are far apart. The right plot of Figure 13 shows the magnitude of the velocity field for M3 and M4 over the “free flow” boundary  $\Gamma_N$ . As expected, M4 presents smaller magnitude values for the oscillations at the end of the channel with respect to M3.

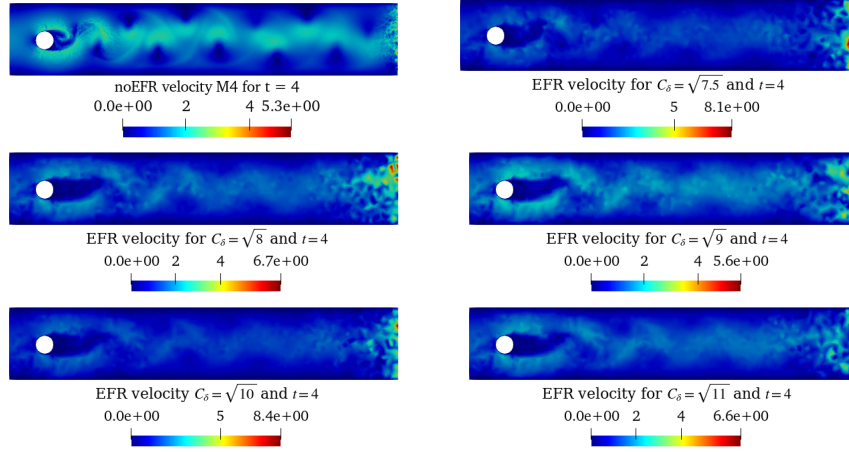


**Figure 14.** Experiment A1. noEFR vs EFR. noEFR over M4 (top left plot) vs EFR over M1 for several values of  $C_\delta$  and  $t = 4$ .

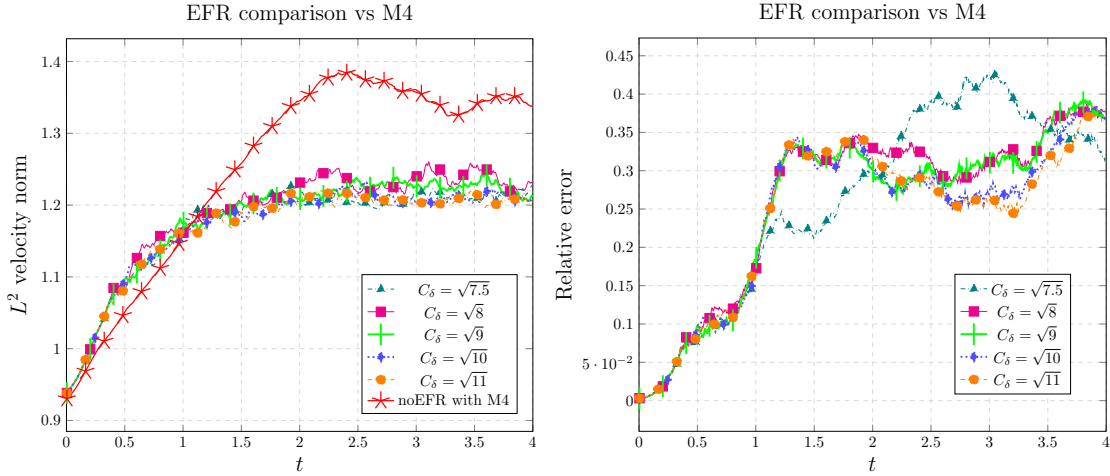


**Figure 15.** Experiment A1. noEFR vs EFR. (left plot)  $L^2$  velocity norm for EFR strategy with  $C_\delta \in \{\sqrt{7.5}, \sqrt{8}, \sqrt{9}, \sqrt{10}, \sqrt{11}\}$ . The results are compared with the noEFR  $L^2$  velocity norm for M4. (Right plot) Relative errors between EFR strategy and M4 with  $C_\delta \in \{\sqrt{7.5}, \sqrt{8}, \sqrt{9}, \sqrt{10}, \sqrt{11}\}$ .

We conclude that M4 is an appropriate choice to accurately represent the flow past a cylinder for  $Re = 1000$ . Thus, we will use M4 as a benchmark to answer the following question: Is it possible to use M1 and EFR to obtain results that are as accurate as those obtained on the finest mesh, M4?

At the FOM level, in the marginally-resolved regime, the EFR algorithm is needed to stabilize the simulation. Indeed, when no EFR algorithm is employed, nonphysical numerical oscillations can be observed for the velocity field, as already shown in the top left plot of Figure 12. In contrast, the EFR algorithm is able to alleviate the oscillations arising in convection-dominated problems and yields more accurate results. Following the suggestions found in, e.g., [15, 71], we use  $\chi = 5 \cdot \Delta t$ . However, we try different values of the differential filter radius,  $\delta$ .

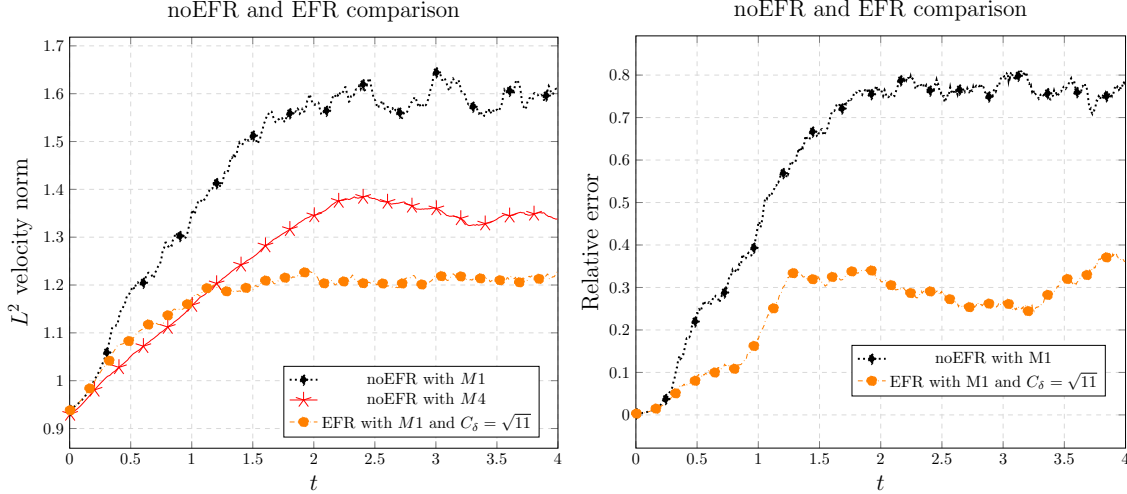


**Figure 16.** Experiment A1. noEFR vs EFR. (left plot)  $L^2$  velocity norm for noEFR and EFR strategies with  $C_\delta = \sqrt{11}$ . The results are compared with the noEFR  $L^2$  velocity norm for M4 (solid starred-red line). (Right plot) Relative errors of noEFR and EFR  $C_\delta = \sqrt{11}$  strategies with respect to the simulation on M4.

We first define a reference value,  $\delta^* = 4.46 \cdot 10^{-3}$ , i.e., the  $h_{min}$  value of M1 (see [71]). Our goal is to increase the action of the differential filter over the domain. To this end, we increase the reference value by a multiplicative constant, i.e., we consider  $\delta = C_\delta \delta^*$ . We try several values for  $C_\delta$  and, for the sake of brevity, we show only the results for  $C_\delta \in \{\sqrt{7.5}, \sqrt{8}, \sqrt{9}, \sqrt{10}, \sqrt{11}\}$ .

All the values are able to recover, with a certain degree of accuracy depending on  $\delta$ , the vortex shedding of the M4 simulation, as shown in Figure 14. With respect to the  $L^2$ -norm of the velocity (left plot of Figure 15), for all the choices of  $C_\delta$ , we obtain comparable results on the entire time interval. These results are very similar to the reference value for  $t \in (0, 1)$ , but are significantly different from the reference value for  $t \in (1, 4)$ . To study the optimal  $\delta$  value, we also investigate the relative error between the EFR strategy and the simulation obtained on the finest mesh, M4 (right plot of Figure 15). This plot shows that  $C_\delta = \sqrt{7.5}$  yields the most accurate results on the time intervals (1, 2) and (3.75, 4), and  $C_\delta = \sqrt{11}$  yields the most accurate results on the time intervals (2.5, 3.75). On the average,  $C_\delta = \sqrt{11}$  seems to yield the most accurate results.

The performance of the EFR strategy with respect to noEFR in terms of  $L^2$  velocity norm and relative error is displayed in Figure 16. These plots show that the EFR regularization is more accurate, with an error that is around 65% smaller for  $t > 1.25$  (right plot) and a better representation of the  $L^2$  velocity norm (left plot).

**A.2. EFR-noEFR vs. EFR-EFR Numerical Comparison (Experiment A2).** In this section, we perform a numerical investigation of the role played by the EFR strategy in under-resolved ROM simulations. To this end, we compare the following two approaches: (i) EFR-noEFR, which is the standard G-ROM without an EFR regularization; and (ii) EFR-EFR, which is the G-ROM with an EFR regularization.

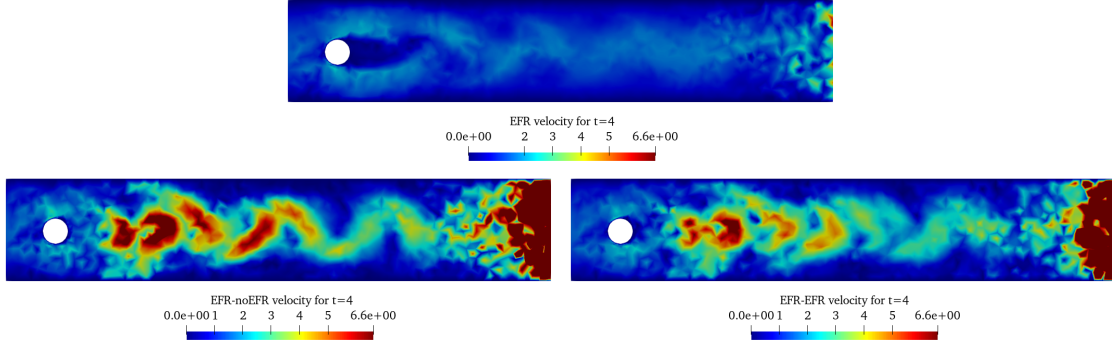


**Figure 17.** Experiment A2. EFR-noEFR vs EFR-EFR. Top plot: EFR velocity profile for  $t = 4$ . Bottom plot: EFR-noEFR (left) and EFR-EFR (right).

**Table 5.** Experiment A2. Information retained by the POD basis functions for velocity and pressure.

$r_u = r_p$	Velocity Information	Pressure Information
5	1%	98%
10	19%	99%
15	26%	99%
20	32%	99%

At the FOM level, we use the EFR strategy presented in section A.1. We recall the parameters used: The triangular mesh parameters are  $h_{min} = 4.46 \cdot 10^{-3}$  and  $h_{max} = 4.02 \cdot 10^{-2}$ , we use a Taylor-Hood  $\mathbb{P}^2 - \mathbb{P}^1$  finite element discretization, and we have  $N_h \doteq N_h^u + N_h^p = 14053$  degrees of freedom. Moreover,  $Re = 1000$ , the time interval is  $(0, 4)$ ,  $\Delta t = 4 \cdot 10^{-4}$ , and  $\delta = C_\delta \delta^*$  with  $C_\delta = \sqrt{11}$  and  $\delta^* = 4.46 \cdot 10^{-3}$ . The relaxation parameter is  $\chi = 5 \cdot \Delta t$ .

For the EFR-EFR algorithm, we follow the consistency strategy proposed in [71] and use the same parameters at the ROM level. We focus on the relative errors of EFR-noEFR and EFR-EFR for velocity and pressure, depicted in Figures 18 and 19, respectively. The errors are computed for several values of the number of modes. For the sake of simplicity, we use  $r = r_u = r_s = r_p \in \{5, 10, 15, 20\}$  obtained by a POD approach over 1000 equispaced snapshots in the time interval  $(0, T)$ . We choose some representative values for the number of basis functions without employing a relative information criterion. Indeed, from Table 5, we see that  $r_u = 20$  is not enough to preserve acceptable values of the relative information of the system. Indeed, in order to represent 98% of the velocity information, a large number of basis functions is needed for the velocity, i.e.,  $r_u = 269$ . For the pressure, a few basis functions are enough to retain 99% of the information. The results, however, are not satisfactory, as depicted in the relative errors plots in Figure 19.

The results in Figures 18 and 19 show that EFR-EFR is more accurate than EFR-noEFR in approximating both the velocity and the pressure (compare the cyan and orange lines or the teal and magenta lines). Thus, our numerical investigation yields the same conclusions and the investigation in [71]: EFR-EFR is more accurate than EFR-noEFR, i.e., using the same type of stabilization at the FOM and ROM levels yields more accurate results. For example, focusing on the velocity profile, for  $r = 10$ , the EFR-EFR error is one order of magnitude lower than the EFR-noEFR error. For  $r = 15$ , the gain is even larger. This is true also for the pressure variable. We note, however, that the relative errors are large. Indeed, numerical oscillations can be observed at the ROM level, as depicted in Figure 17. It is clear that both approaches struggle to represent the EFR solution. The POD retained information and relative error plots suggest that this test problem represents a significant challenge for classical ROM strategies. A different choice for the filter radius and the relaxation parameter at the reduced level could improve the results.

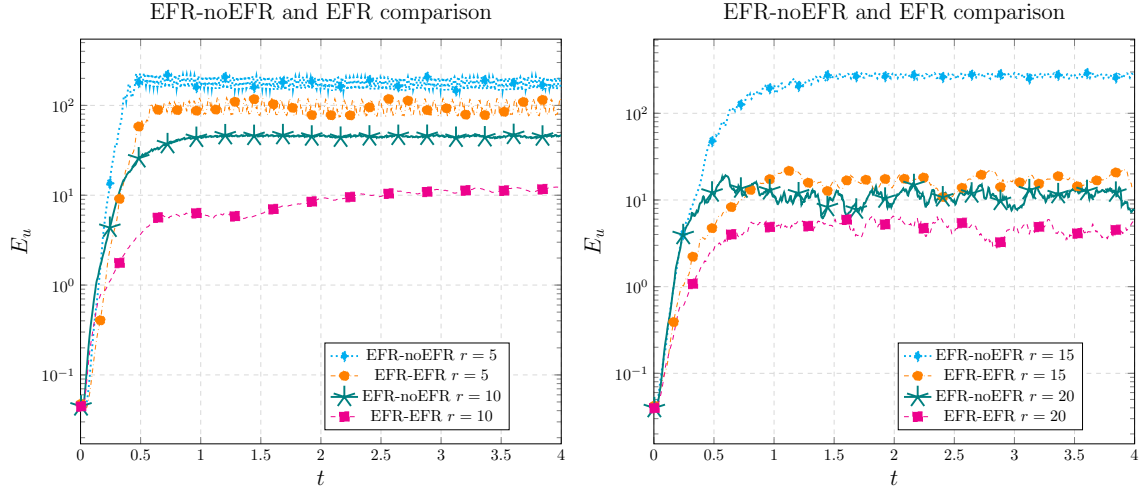


**Figure 18.** Experiment A2. EFR-noEFR vs EFR. Velocity relative error for the EFR-noEFR and EFR strategies with  $C_\delta = \sqrt{11}$  for  $r \in \{5, 10\}$  (left plot) and  $r \in \{15, 20\}$  (right plot).

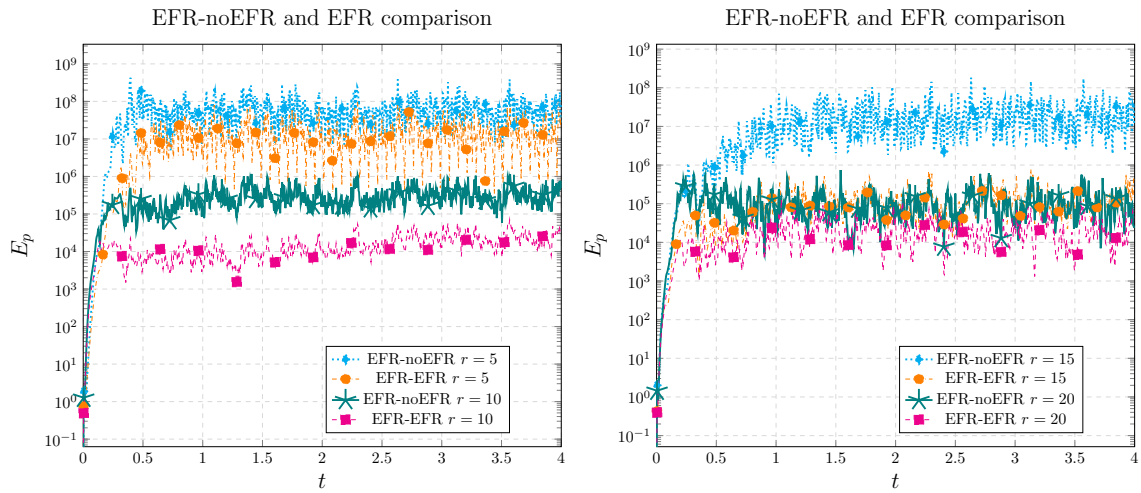


**Figure 19.** Experiment A2. EFR-noEFR vs EFR. Pressure relative error for the EFR-noEFR and EFR strategies with  $C_\delta = \sqrt{11}$  for  $r \in \{5, 10\}$  (left plot) and  $r \in \{15, 20\}$  (right plot).